

7. D. Morrison, T. J. Jones, D. P. Cruikshank, R. E. Murphy, *Icarus* **24**, 157 (1975).
8. M. L. Kaiser, M. D. Desch, J. W. Warwick, J. B. Pearce, *Science* **209**, 1238 (1980).
9. S. A. Collins *et al.*, *Nature (London)* **288**, 439 (1980).
10. Without the dedicated and enthusiastic efforts of a large number of Voyager Project personnel, many of whom spent untold amounts of personal time during evenings and weekends to meet deadlines in a crowded sequence preparation schedule, the successful Saturn encounter of

Voyager 1 would have been impossible. Special thanks are due to J. Diner for her efforts as Saturn Science Coordinator and for her contributions to this overview paper. The Voyager Program is one of the programs of the Planetary Division of NASA's Office of Space Science. The Voyager Project is managed by the Jet Propulsion Laboratory of the California Institute of Technology under NASA contract NAS 7-100.

9 February 1981

## Encounter with Saturn: Voyager 1 Imaging Science Results

**Abstract.** *As Voyager 1 flew through the Saturn system it returned photographs revealing many new and surprising characteristics of this complicated community of bodies. Saturn's atmosphere has numerous, low-contrast, discrete cloud features and a pattern of circulation significantly different from that of Jupiter. Titan is shrouded in a haze layer that varies in thickness and appearance. Among the icy satellites there is considerable variety in density, albedo, and surface morphology and substantial evidence for endogenic surface modification. Trends in density and crater characteristics are quite unlike those of the Galilean satellites. Small inner satellites, three of which were discovered in Voyager images, interact gravitationally with one another and with the ring particles in ways not observed elsewhere in the solar system. Saturn's broad A, B, and C rings contain hundreds of "ringlets," and in the densest portion of the B ring there are numerous nonaxisymmetric features. The narrow F ring has three components which, in at least one instance, are kinked and crisscrossed. Two rings are observed beyond the F ring, and material is seen between the C ring and the planet.*

Saturn is one of the five planets that were known to the ancients. The modern exploration of the system of rings and satellites about this planet began in July 1610 with Galileo's initial telescopic observations (1, 2). Many additional discoveries were made in the 17th century, including Huygens' realization that Saturn was encircled by rings and his discovery of its largest satellite, Titan. The astronomer Cassini discovered Iapetus, Rhea, Dione, and Tethys and first observed the division in the rings that is named after him. He also correctly concluded that the leading hemisphere of Iapetus is much darker than the trailing hemisphere.

Three centuries later, the unmanned U.S. spacecraft Voyager 1 examined the Saturn system at close range with an imaging system (3) that is a direct descendant of the early telescopes of Galileo, Huygens, and Cassini. During its closest approach to Saturn in November 1980, Voyager 1 made observations of the planet and its rings and satellites. Some of the satellites were observed with resolutions approaching 1 km, an improvement of almost three orders of magnitude over ground-based observations and two orders of magnitude over Pioneer 11 images (4). Voyager recorded surface detail for the first time on eight satellites. It discovered several new satellites and revealed hundreds of components of the ring system, perhaps six of which were known previously. In addition,

the images revealed many new phenomena in Saturn's atmosphere. In all, several tens of billions of imaging bits were returned in the few days around closest approach to Saturn—more information than was obtained in the entire previous history of human exploration of this system. This has enabled the greatest leap forward since the 17th century in knowledge about the Saturn system.

**Saturn's atmosphere.** Imaging Saturn is more difficult than imaging Jupiter, both because of the lower intrinsic contrast of features and because of the lower light levels at Saturn's greater distance

from the sun (9.5 versus 5.2 AU). Visually, Saturn's atmosphere differs from Jupiter's in that it has lower contrast and fewer conspicuous features (Fig. 1). Winds are about four times stronger on Saturn, reaching two-thirds the speed of sound near the equator (Fig. 2). Its eastward and westward (zonal) jets are two to four times wider and, unlike Jupiter's jets, bear little relation to its overall banded cloud structure. The external parameters that govern both atmospheres are generally similar; only a few are substantially different. By comparing the dynamics of Jupiter and Saturn's atmospheres we hope to better understand the relative importance of the parameters that influence atmospheric characteristics.

Figure 2 shows measured zonal velocity as a function of planetographic latitude. The measurements were made with the AMOS interactive computing system at Jet Propulsion Laboratory (5) and the MCIDAS system at the University of Wisconsin (6); similar results were obtained at University College London. In generating the Saturn wind profile of Fig. 2 both systems employed user-identified cloud features. Feature position was measured in two frames separated by a known time interval, and the displacement interpreted as a wind vector. Although the possibility of misidentifying wave phase velocities as mass motions (wind vectors) clearly exists, for Jupiter there is no difference between motions of features 50 km in size and those 100 times larger (7). Since atmospheric waves tend to be highly dispersive (phase speed tends to depend on wavelength), this agreement indicates that actual mass motions are being observed. For Saturn we base this assertion on far

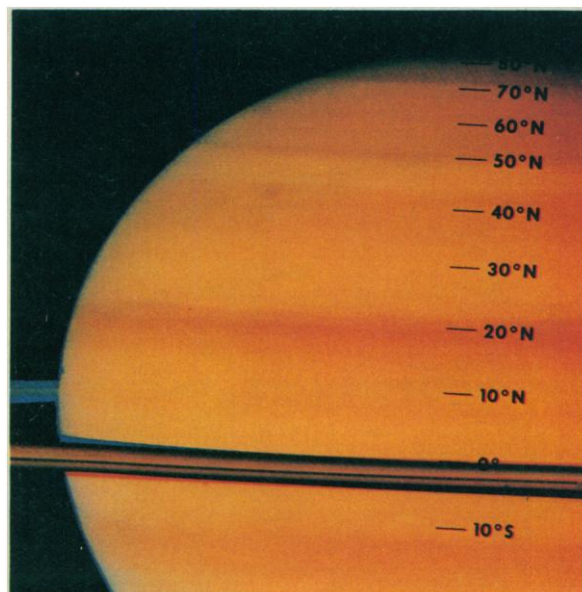


Fig. 1. Color image of Saturn's northern hemisphere. The low contrast is evident when one considers that the part of the planet in the center of the image has more features than any other region on Saturn. The dark North Equatorial Belt is located near 20°N, the more active North Temperate Belt at 40°N. The rings obscure the equator and the region southward. Latitudes are planetographic in all figures.

fewer tie points than for Jupiter (250 versus 15,000). However, our measurements are roughly consistent with the scant ground-based observations of very large-scale features acquired over a period of more than 100 years (8).

Voyager 1 wide-angle images have better signal-to-noise ratios than the nar-

row-angle frames, and the green and orange images show more sharply defined detail than do shorter wavelength (violet or blue) images. The measurements of Fig. 2 were obtained with eight pairs of wide-angle green images and two pairs of orange images. The resolution of the images is roughly 300 km per line pair

(km/lp); the typical time separation is  $10\frac{1}{2}$  hours, or roughly one rotation. Velocities are measured relative to the radio rotation rate, defined here as  $810.76^\circ$  per 24 hours, corresponding to a period of 10 hours 39.4 minutes (9).

The resulting zonal wind profile shows a broad equatorial jet with a peak eastward velocity of about  $480 \text{ m sec}^{-1}$ , roughly two-thirds the speed of sound at 100 K. A westward jet is centered at  $38^\circ\text{N}$  with a maximum velocity of nearly  $30 \text{ m sec}^{-1}$ . A second westward jet may exist at roughly  $55^\circ\text{N}$ ; further evidence for it is the westward-pointing, chevron-like cloud patterns at this latitude in Fig. 3. Perhaps the most startling aspect of Saturn's wind profile is its poor correlation with the belt and zone albedo features, in contrast to the high correlation at Jupiter (see Fig. 4). Virtually no correlation exists at latitudes below  $35^\circ$  in either hemisphere. At higher latitudes (Fig. 3) the middle of the bright and dark bands seem to coincide with the jets, whereas on Jupiter the jets are normally on the band edges.

In westward jets the absolute vorticity gradient with respect to latitude can change sign; that is,  $d^2u/dy^2$  can become larger than  $\beta$ . [Here  $u$  is the eastward velocity,  $y$  is the northward coordinate,  $\beta = (2\Omega/r) \cos \theta$ ,  $\theta$  is the latitude,  $\Omega$  is the planetary rotation frequency, and  $r$  is the planetary radius.] In such regions barotropically unstable flows can occur. In Fig. 2, the solid parabola centered on the westward jet at  $38^\circ\text{N}$  represents the curve of  $d^2u/dy^2 = \beta$ . On the south side of the jet  $d^2u/dy^2 < \beta$ . However, along the north side  $d^2u/dy^2 \geq \beta$ , indicating that some wavelengths may be marginally unstable. It is interesting that many nonzonal cloud features are seen along the north side of this jet (Fig. 5).

Saturn's rather monotonic profile of zonal velocity resembles that observed in the photosphere of the sun more closely than the alternating pattern of eastward and westward jets in the Jovian atmosphere (illustrated by the solid line profile in Fig. 2). Other major differences

Fig. 2. Zonal winds on Saturn and Jupiter. Dots and crosses show the eastward velocity components of individual features in Saturn's atmosphere. The irregular line shows the mean eastward wind profile in Jupiter's atmosphere, an average computed from about 15,000 individual features. The points represented by dots and the profile were obtained with the AMOS interactive image processing system at Jet Propulsion Laboratory (5, 7); the points represented by crosses were obtained with the MCI-DAS system at the University of Wisconsin (6). The solid parabola centered at  $38^\circ\text{N}$  is the curve for which the meridional gradient of absolute vorticity is zero for Saturn. A westward jet with greater curvature than this parabola might be barotropically unstable. On Jupiter, the criterion for instability is exceeded at most of the westward jet locations (7).

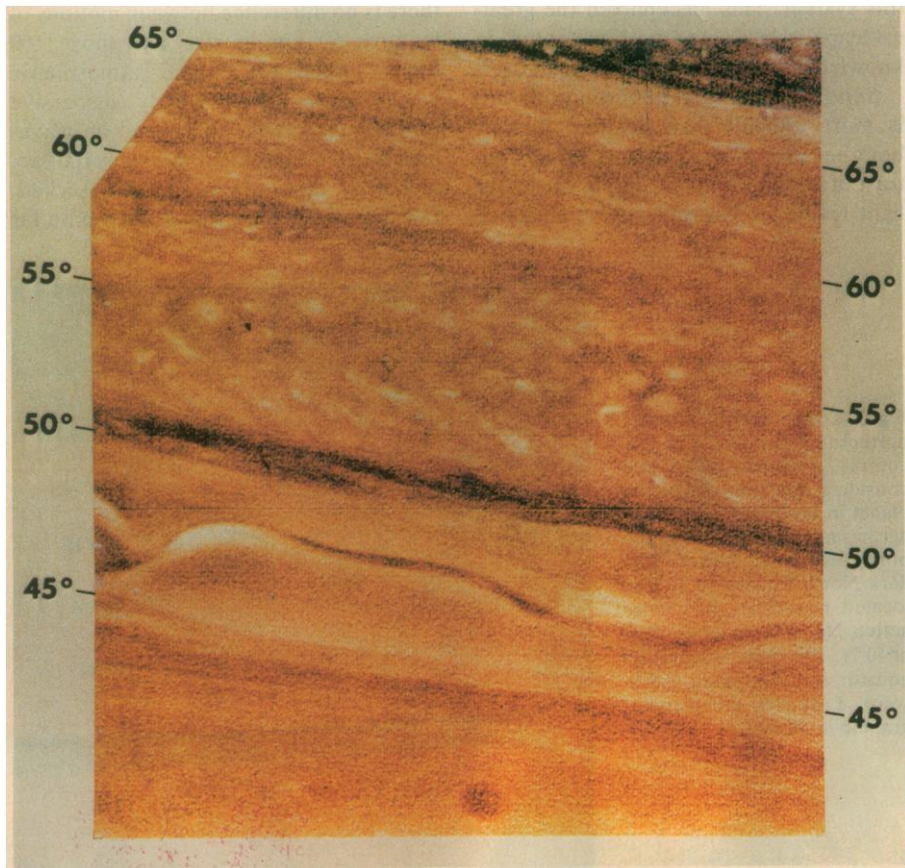
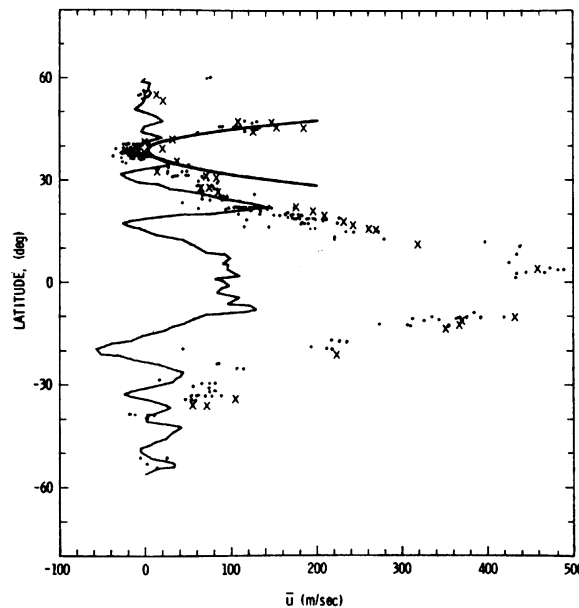


Fig. 3. High-resolution photograph of Saturn's northern hemisphere taken on 10 November 1980 from a range of  $3 \times 10^6 \text{ km}$ . Evidence for alternating zonal jet structure (eastward at  $60^\circ\text{N}$ , westward at  $55^\circ\text{N}$ , eastward at  $50^\circ\text{N}$ ) is seen in the chevronlike pattern centered at  $55^\circ\text{N}$ . The image has been filtered and enhanced to bring out small-scale cloud features. On Jupiter, these features (eddies) are observed to transfer energy into the zonal jets (7). On Saturn such a transfer may also be occurring, but the observational evidence is not yet complete. The resolution of the original photograph is approximately 60 km/lp.

between the two planets are outlined below.

For Jupiter, internal heating supplies less energy to the atmosphere than solar heating, while for Saturn, internal heating supplies roughly twice as much energy as solar heating (10, 11). This internal source would tend to increase the relative importance of small-scale convection on Saturn. The fact that the total energy input to Saturn's atmosphere is only one-third the input to Jupiter's atmosphere leads us to expect smaller convective wind velocities on Saturn. We might also expect the time constant associated with convective motions to be greater. Finally, Saturn's lower gravity leads to a larger atmospheric scale height and a correspondingly larger scale of convective motions. However, the connection between small-scale (10 to 100 km) convection and large-scale ( $\sim 10^4$  km) zonal flows is not obvious.

Models of the interiors of Jupiter and Saturn predict that the depth of the molecular envelope surrounding the liquid

metal core is substantially greater for Saturn—more than half the Saturn radius ( $R_S$ ) (12). If Saturn's zonal wind profile represents the effects of very deep-seated convection extending to the base of the molecular fluid envelope, the horizontal convective scale should be correspondingly greater.

The obliquity of Saturn's rotational axis is approximately  $27^\circ$ , compared to Jupiter's tilt of  $3^\circ$ . At the time of Voyager 1 encounter, it was early spring in Saturn's northern hemisphere. Although it is not clear how seasonal effects might lead to differences in the observed wind profiles, we do not see any obvious hemispheric asymmetries in Saturn's zonal wind profile.

Comparison of Jupiter's zonal velocity profile with its belt and zone pattern of albedo features (Fig. 4, right) gave credence to the widely accepted model of Hadley-type upwelling in zones (with subsequent cooling leading to the formation of ammonia cirrus clouds) and downward motion in belts (with subsequent clearing

rendering visible the darker clouds at a lower level) (13). The correlation between the albedo pattern and the sign of mean zonal shear is that expected for low Rossby numbers; that is, the shear is anticyclonic in zones and cyclonic in belts. For Saturn (Fig. 4, left) there is little correlation between the observed belt and zone pattern and the zonal wind profile. Our studies of the energetics of Jupiter's global circulation indicate that the stresses associated with small-scale eddy motions (scales of roughly  $10^2$  to  $10^3$  km) transport momentum into the mean zonal flow (7), as predicted in pre-Voyager models of Jupiter's atmosphere (14). Thus Hadley-type overturning is not required to explain the Jovian zonal wind profile. Still, the old notion of rising zones and sinking belts is not easily laid to rest in light of the overall correlation between albedo and shear on Jupiter. The observation of a similar belt and zone pattern on Saturn with a very dissimilar zonal wind profile clearly suggests that the long-accepted model is

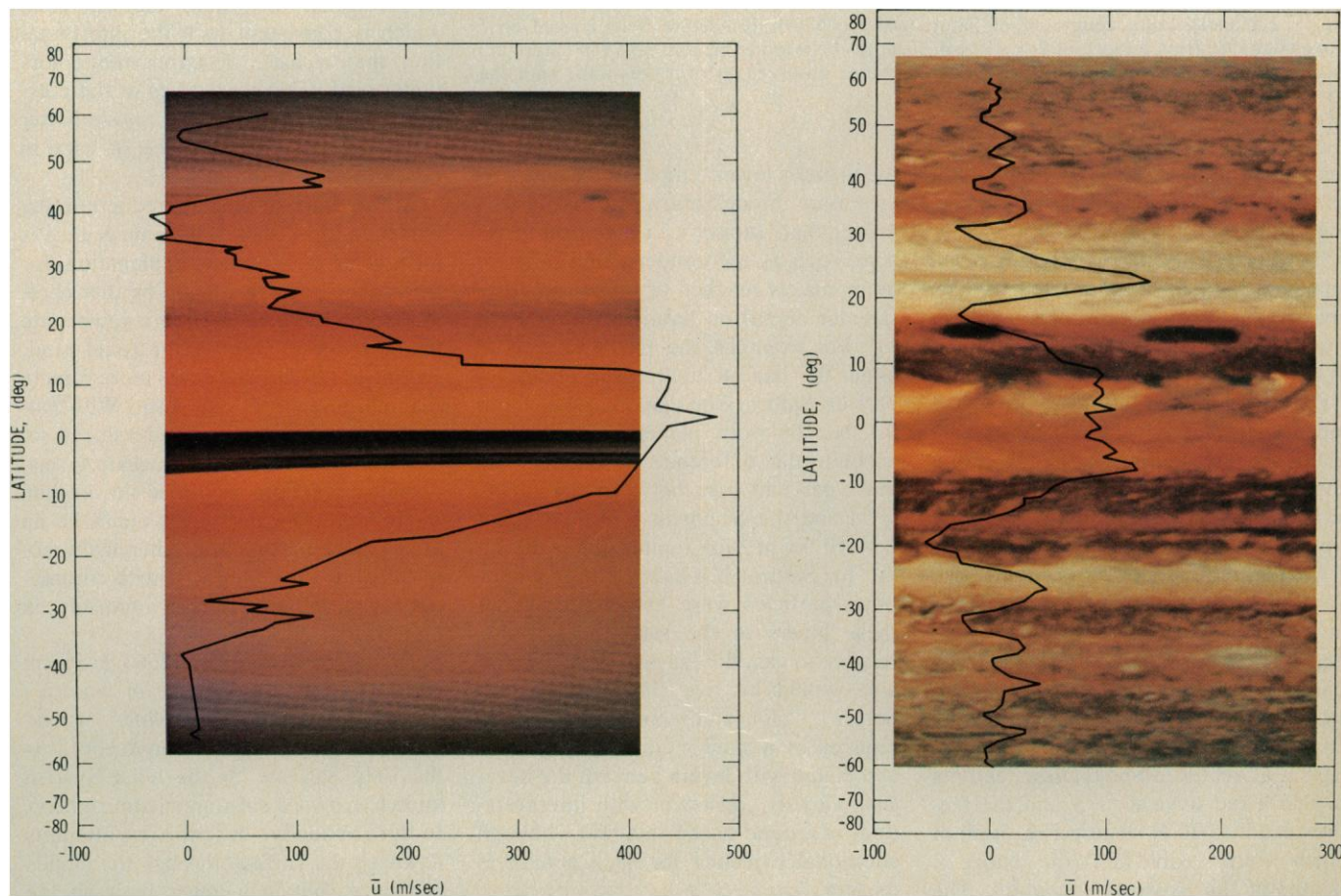


Fig. 4. (Left) profile of Saturn's mean eastward winds, measured relative to the radio period of 10 hours 39.4 minutes, overlaid on a cylindrically projected Saturn color composite. There is little correlation between the belt and zone albedo cloud patterns and the zonal wind profile. The rings obscure the equator and an area somewhat southward, so the curve has been interpolated in this region. (Right) Profile of Jupiter's mean eastward winds, measured relative to the radio period of 9 hours 55.5 minutes, overlaid on a cylindrically projected color composite of Jupiter. Note the association of belts (darker bands) with cyclonic shear (northwest-southeast tilt in the northern hemisphere, northeast-southwest tilt in the southern hemisphere) and of zones (lighter bands) with anticyclonic shear. The region  $23^\circ$  to  $31^\circ$ N was abnormally light at the time the color composite was taken. [Projections prepared by G. W. Garneau, JPL Image Processing Laboratory]

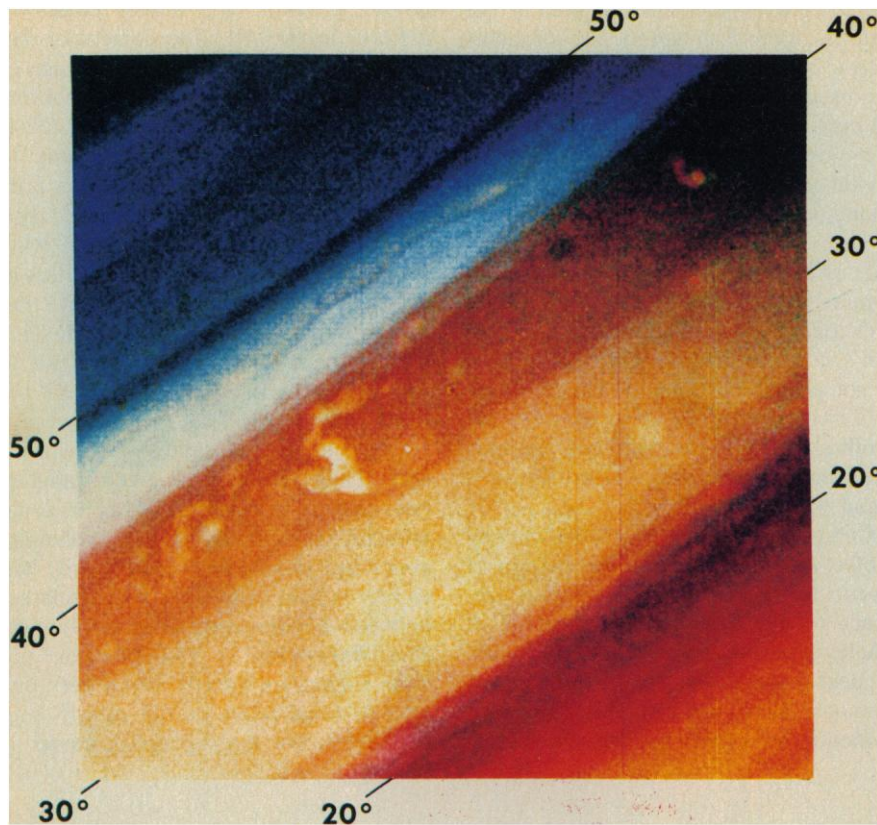


Fig. 5. Enhanced color composite of Saturn's active North Temperate Belt, imaged on 5 November 1980 from a range of  $9 \times 10^6$  km. Features believed to be convective in nature are seen near the center of the belt. These features are observed to drift westward with the prevailing westward jet at  $38^\circ\text{N}$ .

incomplete. The mean motions in the solar photosphere are, like Jupiter's, maintained by the smaller-scale eddy motions (15). The similarity between the solar and Saturnian zonal wind profiles suggests that eddy stresses also maintain the mean flow on Saturn. The amplitude of the equatorial jet suggests an abundance of vigorous eddies; yet the visual appearance of the planet suggests that eddies are rare. Perhaps a thick haze or a relative lack of atmospheric colored compounds (chromophores) renders the driving eddies invisible on Saturn.

Another difference between the two planets is the scarcity of large oval spots on Saturn. Features with diameters greater than 1000 km are at least ten times as abundant on Jupiter. The largest such features observed on Saturn by Voyager 1 are about one-tenth the size of Jupiter's Great Red Spot. These features include a red oval at  $55^\circ\text{S}$  and the features at  $25^\circ$  to  $40^\circ\text{N}$  seen in Fig. 5, all of which were visible for the entire 3 months of the Voyager encounter. The same features are just to the left of center in Fig. 1, but are essentially invisible without the extreme contrast enhancement of Fig. 5.

The lower contrast of features on Saturn (Figs. 1 and 6) is explained in part by

the planet's lower temperatures and lower gravity. Since Saturn's atmosphere is colder than Jupiter's, a given temperature, such as the condensation point of ammonia, is reached at higher pressure (greater depth) on Saturn than on Jupiter. For example, the 150 K level is at about 0.7 bar on Jupiter and about 1.4 bars on Saturn. The tropopause is about 0.1 bar on both planets. Taking into account the difference in gravity, the mass per unit area between the 150 K level and the tropopause is then about  $2 \times 10^3 \text{ kg m}^{-2}$  for Jupiter and  $\sim 10^4 \text{ kg m}^{-2}$  for Saturn. If a haze of ammonia or other particles were mixed throughout these layers in the same mass ratios relative to gas, the mass of haze per unit area would be five times greater for Saturn. Color and contrast would be reduced by a similar factor if they were associated with layers beneath the haze. This view is consistent with interpretations of ground-based data (16), although additional evidence for such a haze is meager.

Molecular scattering above the main cloud tops is also greater in Saturn's atmosphere than in Jupiter's by a factor of 4 or 5. Because Rayleigh scattering depends on wavelength ( $\lambda$ ) as  $\lambda^{-4}$ , it cannot explain the loss of contrast at

long wavelengths. However, in the North Equatorial Belt (NEB) we observe the signature of such molecular scattering as a contrast reversal between features seen in the violet and ultraviolet filters at 4100 and 3500 Å, respectively. The NEB is 15 percent darker than average in the violet but appears brighter by the same amount in the ultraviolet. The albedo is low,  $I/F \sim 0.2$ , at these wavelengths (17, 18), so the Rayleigh scattering optical depths cannot be greater than about 0.1 or 0.2. The areas that are darker in violet must have Rayleigh scattering optical depths about 0.1 greater than bright areas. Thus there must be about  $0.6 \times 10^3 \text{ kg m}^{-2}$  more hydrogen gas above the areas that are dark at violet and longer wavelengths, corresponding to a pressure difference of about 0.15 bar. These extremely rough estimates imply that the NEB is lower in the atmosphere or has less haze above it than the bright areas.

The contrast reversal is also seen in views of the crescent at scattering angles around  $60^\circ$  (Fig. 7). At longer wavelengths the crescent shows somewhat less contrast than does the full disk, which is consistent with the interpretation that a haze obscures the colors underneath. Further studies of the crescent and the limb should provide better estimates of the importance of haze in obscuring the features.

At this stage in the data reduction, the evidence for a thicker haze on Saturn is inconclusive. Another explanation for the reduced contrast might be that chromophores are generated at a lower rate than the rate of shear of the zonal wind, so that eddies are dispersed more rapidly than chromophores can form. With Saturn's lower temperature and reduced solar flux, particularly at cloud-top levels, chemical reactions would be slower than on Jupiter. The net result could be an atmosphere that is more chemically homogeneous than Jupiter's, with chromophores distributed more uniformly in latitude.

*Titan.* With a radius of  $2560 \pm 26$  km (19), Titan is the largest of Saturn's moons and, among all satellites, second in size only to Jupiter's Ganymede. It is the only satellite in the solar system known to have a substantial atmosphere. In this section we describe our attempts to image the surface through the clouds and haze, obtain a lower limit on the optical thickness and an estimate of particle size, and discuss the altitudes of the clouds and haze and compare our estimates based on Voyager imaging with results obtained by other means. We close with a discussion of low-contrast

features observed on the disk: the north-south brightness difference, the mid-latitude banding, and the dark polar hood.

The first compelling evidence for Titan's atmosphere was Kuiper's (20) spectroscopic discovery of methane. Ground-based (21, 22), Earth-orbiting satellite (23), and Pioneer 11 (4) imaging all provided strong evidence for an optically thick atmosphere. The obscuration may be due to a molecular photochemical smog (24) or aerosols. An effort was made to find breaks in the clouds in Voyager images. During the several hours before Titan closest approach we were able to mosaic 90 percent of the illuminated disk at resolutions better than 3.4 km/lp and 50 percent at better than 1.3 km/lp. We could detect no breaks in the clouds (see Fig. 8).

Lower limits of the optical depth,  $\tau$ , of the aerosols in Titan's atmosphere can be estimated by attributing the lack of small-scale contrast—readily seen on all other satellites in the Saturn system—to aerosol obscuration. We employ for the Titan aerosols the multiple-scattering model of Rages and Pollack (25). If we assume that the albedo variations on Titan's surface are comparable to those on the surface of Iapetus (0.05 to 0.50) and use an upper boundary of a few percent for the contrast on Titan frames, we derive  $\tau > 10$  for the visible optical depth of the atmospheric aerosols. A more realistic range for surface albedos of 0.35 to 0.50, such as occurs on the surfaces of many of the inner satellites of Saturn, yields  $\tau > 5$ . Thus the aerosol layer is quite opaque in the visible, with an optical depth at least as great as that on Mars at the height of a global dust storm. On the other hand, at 20  $\mu\text{m}$  the aerosols may be transparent (10).

We estimated the cross-sectionally weighted mean radius  $\bar{r}$  of the aerosol particles from the change in brightness of Titan at high phase angles (small scattering angles). At these angles the single-scattering phase function is dominated by diffraction, becomes progressively narrower and sharper as  $\bar{r}$  increases, and is relatively insensitive to particle shape (26). At a wavelength of 0.42  $\mu\text{m}$ , the brightness ratio of Titan at phase angles of 160° and 129° is  $\approx 5$  for the main haze layer close to the equatorial limb. Simulations of these results with a multiple-scattering model of the aerosol layer (25) indicate that  $\bar{r} \sim 0.3 \mu\text{m}$ .

Our estimate of  $\bar{r}$  near the top of the main haze layer can be compared with other estimates. Assuming that the aerosols could be modeled as spherical particles, Tomasko (27) simulated Pioneer 11 polarization measurements and found

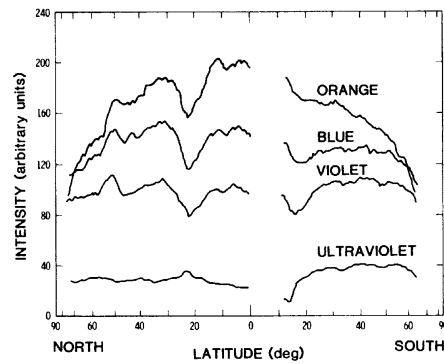


Fig. 6. Pole-to-pole intensity scans of Saturn in four colors. The four curves have a common zero but different intensity scales proportional to raw data numbers uncorrected for scattering geometry. Values of  $I/F \times 10^3$  (17) may be obtained by multiplying the ordinate values by 3.0, 2.5, 2.2, or 6.5 for the orange, blue, violet, or ultraviolet filters, respectively. Note the generally low contrast ( $\pm 10$  percent) as well as the ultraviolet contrast reversal of the prominent belt at 21°N. The region from 0° to 12°S is not shown in the scans because of the presence of the rings.

$\bar{r} \sim 0.08 \mu\text{m}$ . Particles of this size imply a brightness ratio of only about 1.5 for phase angles of 160° and 129°, which is incompatible with the observed ratio. Conceivably, the polarization data can be reconciled with our results if allowance is made for nonsphericity of the particles—either in their shape or their surface microstructure. Our value for  $\bar{r}$  is in crude agreement with the values obtained from the brightness variation of Titan at the very small phase angles accessible from Earth (25).

High-resolution views of the limb at high phase angles reveal an optically thin layer of haze  $\sim 50$  km thick roughly 100 km above the main aerosol layer. The haze was initially thought to be separate from the main aerosol deck, but photometric analysis of Voyager images shows some aerosol material between the two

layers. The haze layer extends from the top of the north polar hood entirely around the illuminated hemisphere, continuing some distance beyond the terminator in both hemispheres (Fig. 9). Over a short range of longitudes, it exhibits a fine structure of subsidiary but not discrete layers (Fig. 10).

Intensity profiles of Titan's limb produced from Voyager images show an inflection between 2765 and 2796 km from the center of Titan, corresponding to the main haze layer, and a peak between 2805 and 2845 km, corresponding to the center of the higher haze layer (Fig. 11). From Pioneer 11 experiments with much inferior resolution, the visible radius of Titan was estimated as  $2860 \pm 20$  km (28), assuming a brightness step function at the limb. Because the Pioneer experiments were unable to resolve the haze layer, their results seem to be in good accord with our measurements. The air mass through the tangential light path to the limb is  $\sim 20$ . Thus the equivalent normal-incidence optical depth corresponding to the optical limb (photometric inflection) is at  $\tau \sim 0.05$ . Therefore, the optical limb is about 240 km above the solid surface determined by the Voyager 1 radio occultation experiment (19).

The Voyager 1 ultraviolet spectrometer detected discrete absorbing layers (29) at mean radii of 3335 and 2966 km. The results indicate that the source of extinction in the higher layer is probably molecular rather than particulate, and that in the lower layer may also be molecular rather than particulate. Since the ultraviolet instrument experienced a cutoff of 2886 km on ingress and 2869 km on egress, its lack of detection of the optical haze layer diagrammed in Fig. 11 does not contradict the imaging data.

It is also interesting to compare our

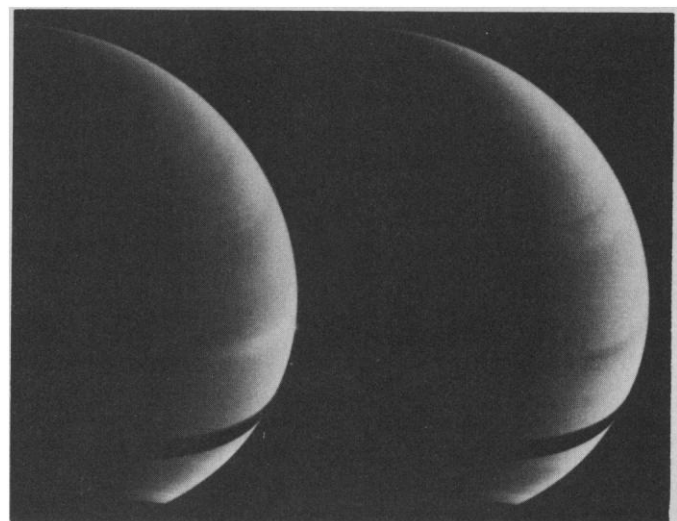


Fig. 7. Crescent photographs of Saturn in the ultraviolet (left) and violet (right) filters. Note the contrast reversal of the belt located near the middle of the limb. The photographs were taken at a phase angle of approximately 118° (scattering angle approximately 62°).

measured limb radius with that obtained by combining ground-based spectroscopic estimates (30–32) of cloud pressure with the pressure-radius curve obtained from Voyager infrared and radio science observations (10, 19). Hunten's (32) temperature-pressure curve, obtained by comparing strong and weak methane absorption bands in Titan's atmosphere, agrees well with the Voyager infrared and radio science curve (Fig. 11). However, Hunten placed the effective pressure of optical penetration in the range 300 to 900 mbar, the latter implying a limb pressure of 10 to 50 mbar. The Voyager optical limb is near the 0.2-mbar level. It is possible that this represents still another haze layer overlying Hunten's main cloud. If so, the level of visual penetration attained in pictures of Titan taken near full phase (Fig. 8) is close to the top of the convective region of the atmosphere, as expected from first principles (33).

Color images of Titan show a reddish disk with a readily discernible interhemispheric asymmetry: the southern hemisphere is of relatively uniform brightness; the northern hemisphere is darker and redder and is surmounted by a still darker north polar hood (Fig. 8). Extreme contrast enhancement (Fig. 8) reveals several distinctive, zonally organized features, reminiscent of the zones and belts in the Jovian and Saturnian cloud systems. The interhemispheric boundary lies in Titan's orbital plane (probable error,  $\pm 5^\circ$ ). This symmetry

plane is almost certainly determined solely by Titan's rotation. This represents the first determination of the obliquity of Titan, namely  $0^\circ \pm 5^\circ$ . North of the equator are two broad dark belts with possible substructure. A thin bright zone separates the protuberant north polar hood from the darker belt to the south, which extends southward from  $\sim 65^\circ$ . There is no hint of a south polar hood.

Notwithstanding our observation of a limb at about 0.2 mbar, the possibility that the penetration attained over most of the disk in images taken near full phase may be much deeper suggests that the interhemispheric asymmetry may be caused by a difference in the height or particle number density of the underlying condensation clouds, such that there is a brighter white substrate in the southern than in the northern hemisphere. Alternatively, the asymmetry may be caused by variations in particle size or composition of the dark, presumably organic, aerosols that color its haze and clouds. Particle-size modulation might arise from aerosol variations in the energy sources converting atmospheric  $\text{CH}_4$  and  $\text{N}_2$  to organic materials, or from additional condensation at the poles of intermediate-carbon-number organic matter. Composition modulation might arise from periodic variations in the flux of charged particles in the Saturnian magnetosphere as Titan bobs in and out of the planet's magnetopause. No current model fully explains Titan's interhemispheric albedo asymmetry or

the presence of a polar hood only in its northern hemisphere.

On the other hand, the asymmetry may be dynamical in origin, caused by seasonal variations in the distribution of solar heating. Thermally forced circulation differences between winter and summer hemispheres may produce differences in cloud density, altitude, and composition that result in different albedos. An analogous effect occurs on Earth, with the winter hemisphere tending to be brighter due to more stratus cloud and ice and snow cover. Although the brightness asymmetry was observed by Voyager shortly after Titan's equinox, when solar input to the two hemispheres is nearly symmetrical, Titan has a very long radiative time constant,  $\tau$  (ratio of the atmospheric thermal energy content to the mean solar heating rate for the atmosphere). With a  $\text{N}_2$  atmosphere (19, 29) and the Voyager radio science surface pressure and temperature, we find  $\tau = 138$  years, roughly 400 times the value for Earth's atmosphere. Since the period of solar thermal forcing is equal to Saturn's orbital period of 29.5 years, the thermal response of Titan's atmosphere will lag by a phase angle  $\sim \arctan(2\pi \times 138/29.5) = 88^\circ$ . The lag is almost exactly one season ( $90^\circ$ ). Thus the maximum thermal gradient between Titan's northern and southern hemispheres should occur at the equinoxes, not at the solstices, and at the time of the Voyager 1 encounter the effective atmospheric season would be just past midwinter.

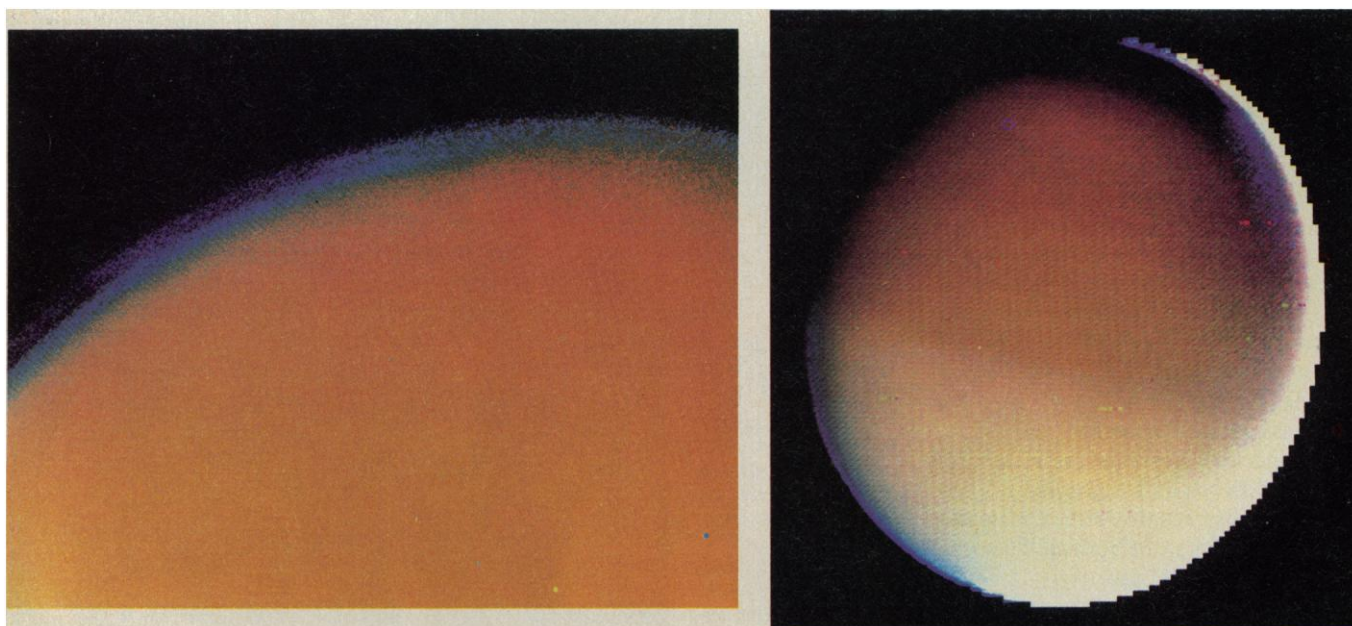


Fig. 8. (Left) Far-encounter image of Titan, showing the protuberant north polar hood. The reddish color of the clouds is thought to be due to complex organic molecules. (Right) Severely contrast-enhanced image of Titan, corrected by a Minnaert photometric function, which is responsible for the step-function artifact at the right limb. Zonal structure in the northern hemisphere clouds is revealed, consisting primarily of a low-albedo northern mid-latitude band, brightening before the onset of the polar hood at latitudes of  $\sim 65^\circ$ . There is a hint of subsidiary structure as well. The colors are exaggerated in both images.

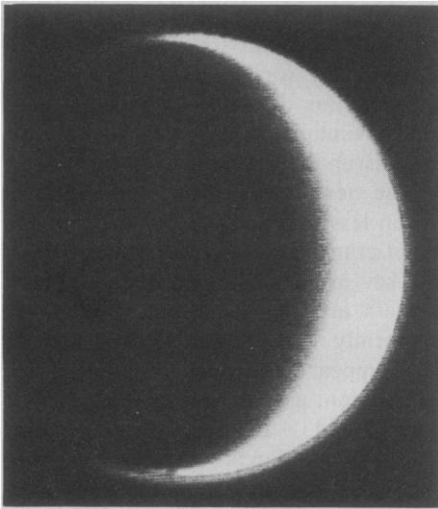


Fig. 9. The global extent of Titan's haze layer can be seen in this high phase angle ( $129^\circ$ ), narrow-angle photograph, taken on 13 November 1980 from a distance of  $2.3 \times 10^6$  km (resolution, 43 km/lp).

The  $90^\circ$  phase shift of seasons on Titan may also allow a seasonal interpretation of the secular brightening of Titan observed by Lockwood (34) since 1972. The fact that the brightening continued through May 1973 southern summer solstice, originally used to reject this interpretation, may be consistent with it.

If we assume that the albedo of each hemisphere varies sinusoidally between a maximum at the autumnal equinox and a minimum at the vernal equinox and that, due to the inclination of Titan's spin axis (to the ecliptic, not to its own orbital plane), the fraction of each hemisphere seen from Earth varies sinusoidally from a minimum at winter solstice to a maximum at summer solstice, then we can model the modulation of apparent brightness of the southern hemisphere by  $[1 + a \sin(\omega t')] [1 + f \cos(\omega t')]$  and of the northern hemisphere by  $[1 - a \sin(\omega t')] [1 - f \cos(\omega t')]$ , where  $a$  is the half-amplitude of the hemisphere brightness variation,  $f$  the half-amplitude of the hemisphere weighting variation,  $\omega$  the orbital frequency of Saturn, and  $t'$  the time from the 1973 southern summer solstice. The instantaneous mean brightness of Titan as a whole is thus proportional to  $1 + af \sin(2\omega t')$ .

This model implies a geometric albedo variation at twice the Saturn orbital frequency, with extremes of brightness midway between solstice and equinox. The last minimum would have occurred at  $2\omega t' = -\pi/2$ , about 3.5 years before the mid-1973 solstice, and the last maximum at  $2\omega t' = +\pi/2$ , about 3.5 years after the mid-1973 solstice. These values are consistent with the increase observed since 1972, provided  $af \approx 0.7$

(34). If  $f$  is approximated by the sine of the inclination angle of Titan's axis, then  $a \approx 0.15$ . This implies a maximum brightness ratio between summer and winter hemispheres of  $(1 + 0.15)/(1 - 0.15) = 1.35$ , which occurs at the equinoxes. Preliminary photometric data from Voyager frames taken through a blue filter yield a contrast ratio between the northern and southern hemispheres of  $\sim 1.20$ . Considering the approximate nature of the calculation above, it may be consistent with the data. The secular brightening of Titan has a wavelength dependence; it is not yet clear if the interhemispheric contrast in the Voyager images shows a consistent wavelength dependence.

Lockwood (35) reported that Titan reached its maximum brightness in 1976 and 1977, almost exactly as this model predicts, and has since been decreasing in brightness at 2 percent per year. He suspected a correlation with solar activity and predicted a minimum brightness in 1981 and 1982 (35). The model proposed here predicts a minimum in 1983 and 1984. Discrimination between these two models by ground-based observations should be possible in the next 3 to 4 years. If our model proves valid, it leaves open the question of why Neptune shows the same phase relationship as Titan, consistent with a solar variation model.

Titan is probably tidally locked to Saturn; its day is then equal to its orbital period, about 16 Earth days, implying a zonally symmetric thermal forcing. Because the time constant for meridional



Fig. 10. Several haze layers can be seen in this unique image of the limb of Titan, taken on 12 November 1980, at a range of 4000 km, 5 minutes after closest approach to Titan. The height of the region shown in this figure is about 220 km and the image has been substantially increased in contrast.

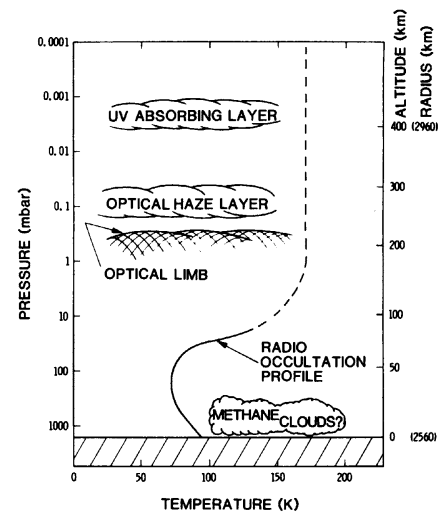


Fig. 11. Schematic representation of the structure of Titan's atmosphere and the disposition of aerosols and clouds, based on Voyager 1 optical, ultraviolet, infrared, and microwave experiments. A thermal inversion is expected at high altitudes. Fine structure in the haze layers has been suppressed.

motions is probably comparable to  $t$ , Titan's rotation may play a significant dynamical role in these motions. Finally, scaling considerations suggest (36) that a weak zonally symmetric circulation is more likely than a wave regime for Titan. This may explain the zonal symmetry of the brightness variations of Titan, although the observed latitudinal variations remain unexplained.

Finally, we note that the Voyager observations are relevant to previous ground-based observations of detail on the disk of Titan. A series of drawings based on ground-based observations show large variations in the appearance of the satellite as a function of its orbital position (2). No single drawing accurately reproduces the appearance of Titan as seen by Voyager 1. It might be argued that the spacecraft viewed Titan during an anomalous period, but our analysis of the atmospheric dynamics suggests that it did not. We conclude that the small angular size of Titan may have misled ground-based observers.

*Icy satellites.* The Saturn system is one of the three known systems of regular satellites; the others are those of Uranus and the inner satellites of Jupiter. (Regular satellites are those with nearly circular direct orbits in the primary planet's equatorial plane.) All three planets with regular satellite systems are now known to have ring systems as well. Theoretical models suggest that such systems are a common consequence of planet formation—each system of planet, rings, and regular satellites a miniature solar system. By "icy satellites" we mean the large, atmosphere-free Saturni-

Table 1. Bulk properties of the largest Saturnian satellites.

Satellite	Orbit radius ( $R_S$ )	Radius* (km)	Density† ( $g\ cm^{-3}$ )	Geometric‡ albedo
Mimas (S1)	3.08	195 ± 5	1.2 ± 0.1	0.6 ± 0.1
Enceladus (S2)	3.97	250 ± 10	1.1 ± 0.6	1.0 ± 0.1
Tethys (S3)	4.91	525 ± 10	1.0 ± 0.1	0.8 ± 0.1
Dione (S4)	6.29	560 ± 10	1.4 ± 0.1	0.6 ± 0.1
Rhea (S5)	8.78	765 ± 10	1.3 ± 0.1	0.6 ± 0.1
Titan (S6)	20.4	2560 ± 26	1.9 ± 0.06	
Hyperion (S7)	24.7	145 ± 20		0.3 ± 0.1
Iapetus (S8)	59.3	720 ± 20	1.2 ± 0.5	0.5 ± 0.3 (bright side)

\*Average from several independent limb-fitting routines to Voyager 1 images, except Titan, which is from Tyler *et al.* (19). †Masses for Rhea and Titan are from Tyler *et al.* (19); others are from ground-based (38) and Pioneer (39) measurements. ‡Albedos derived from telescopic visual magnitudes (37, 38) and Voyager 1 radii determinations.

an satellites. We thus include Mimas (S1), Enceladus (S2), Tethys (S3), Dione (S4), Rhea (S5), Hyperion (S7), Iapetus (S8), and Phoebe (S9), but exclude Titan. All of these satellites, except Iapetus, Phoebe, and possibly Hyperion, are regular satellites. Throughout this section "ice" refers to water ice unless otherwise specified.

Analysis of ground-based data indicated that most, if not all, of the icy satellites are low-density (1 to 2  $g\ cm^{-3}$ ), bright objects (geometric albedo generally  $\sim 0.4$ ) (37). Infrared photometry and spectroscopy established that most of these satellites, and the bright hemisphere of Iapetus, are at least partly covered with water frost or ice (38).

Before the Voyager 1 encounter with Saturn we had far less information about its satellites than we did about Jupiter's before 1979. This was due to Saturn's greater distance from Earth and the sun, the smaller diameter of its satellites, and their closeness to Saturn. Only Titan is comparable in size with the Galilean satellites. The icy satellites are intermediate in size between the largest asteroids and the moon. Voyager 1 provided the first close look at bodies in this size range.

Voyager 1 obtained high-quality images of most of the previously known satellites. Mimas, Dione, and Rhea were observed at a range of less than 200,000 km, and pictures were acquired with resolutions of 4.0 km/lp or better. Rhea was observed at a range of only 59,000 km with a resolution of 1.3 km/lp. Voyager 2 will view these objects at much lower resolution. Enceladus, Tethys, Iapetus, and Hyperion were observed at much lower resolution by Voyager 1, but will be studied at closer range during the Voyager 2 encounter in August 1981.

Basic properties of the large Saturnian satellites (Table 1) agree, within the stated errors, with previous estimates from ground-based measurements (37). The

uncertainties in the radii are much smaller than those in previous estimates and allow calculation of meaningful densities (where masses are known) and mean geometric albedos. These data bear out the pre-Voyager estimate (39) that most of these satellites are very bright, low-density bodies. The satellites vary, however, in albedo and density. Enceladus and Tethys appear brighter than the other satellites and seem to be less dense (although the mass of Enceladus is still poorly determined). The best Voyager 1 global views of the six large icy satellites are shown in Fig. 12, printed to correct linear scale with average brightnesses approximately scaled to the true albedos.

Preliminary maps of Dione, Rhea, Tethys, and Mimas showing albedo markings and topographic features are shown in Fig. 13. Perspective projections of latitude and longitude were prepared for each frame (unrectified), based on the position and orientation of the satellite with respect to the spacecraft. Map details were then transferred from the perspective view to Mercator and polar stereographic projections by airbrush cartographic techniques. The resulting maps vary in detail in accordance with the resolution of the photographic coverage. They will be improved as precise coordinates of control points become available and updated with new positional information and Voyager 2 data.

*Mimas.* The most striking feature on Mimas, the smallest and innermost satellite, is a giant crater roughly 130 km in diameter (Fig. 14, left), nearly centered on the leading hemisphere (Fig. 13). The crater walls have an estimated average height of 5 km, and parts of the floor may be more than 10 km deep. An enormous central peak, 20 by 30 km at its base, rises about 6 km from the crater floor and was probably generated by a rebound of the floor under the extremely weak gravity of Mimas ( $\sim 0.005$  that of Earth). The diameter of the crater is

about one-third the diameter of the satellite. For a body the size of Mimas, which is relatively weakly bound by its own gravity, this diameter is probably near the maximum that can be produced without disrupting the body.

The next largest crater on Mimas is much less than half the diameter of the giant crater, and few craters larger than 50 km in diameter are seen. Smaller craters are abundant and, in general, uniformly distributed, although there does appear to be some variation in this population, as seen in the shaded relief map (Fig. 13). The region in the central part of the Mercator projection, from 40°W eastward to 260°W (best viewed in Fig. 14, right), has very few craters in the 20- to 50-km size range, whereas the region from 260°W eastward to the giant crater at 100°W (Fig. 14, left) has a substantial number. The transition between the two regions occurs near the antapex of orbital motion and is therefore probably not simply a result of variation in cratering flux from leading to trailing hemisphere. Conceivably, the intermediate axis of the ellipsoid, which coincides with the apex of motion, was shifted by an impact or impacts. Alternatively, the region with few 20- to 50-km craters may have a younger surface, on which later processes obliterated preexisting large craters.

Most of the craters are approximately bowl-shaped and much deeper than craters of comparable size on the moon or the icy Galilean satellites. The greater depths are probably due to the extremely low gravity field. Craters  $\geq 20$  km in diameter contain rudimentary central peaks. Craters commonly are superposed on other craters, and many of the older craters are severely degraded. No ray craters have been recognized, possibly because of the intrinsically high albedo of the mature surface. The high and relatively uniform crater density and the great range in degree of crater preservation across the satellite indicate that the population of craters with diameters  $\leq 30$  km is generally in equilibrium (craters formed and destroyed at the same rate). The giant crater near the apex is relatively unmodified by superposed craters and is evidently younger than most of the rest of the surface.

In addition to craters, the surface of Mimas is scored by grooves as much as 90 km long and generally about 10 km wide and 1 to 2 km deep. They are best seen in the southern Saturn-facing hemisphere, where the highest resolution images were obtained. The most conspicuous grooves trend northwest and west-northwest. Some are straight and may

have formed over deep-seated fractures or fracture systems; others are less regular and may consist of chains of coalesced craters. The grooves may have been produced when the giant crater at the apex was formed, or they may have been developed by tidal interactions as the body cooled and froze (if it was, in fact, ever warm and mobile). Also present in the trailing hemisphere are local clusters of hills, which are commonly

about 5 to 10 km across and  $\leq 1$  km high. They may consist of coarse blocky ejecta from the giant crater.

Preliminary radiometric reduction of a Voyager 1 image at a phase angle of  $43^\circ$  gives brightness values  $I/F$  (17) ranging from 0.45 to 0.50 for bright regions on Mimas. This range is consistent with a surface coated with water frost and with the average albedo given in Table 1.

*Enceladus*. Mimas and Enceladus

form a pair in terms of diameter (390 and 500 km); the next larger pair, Tethys and Dione, are an order of magnitude more massive. Enceladus appears to have a smoother surface than the other satellites, although its photographic coverage is poorer. The closest pictures were taken at a range of 622,000 km and have a resolution of 11 km/lp. On other satellites, craters are visible in pictures with comparable resolution, but none can be

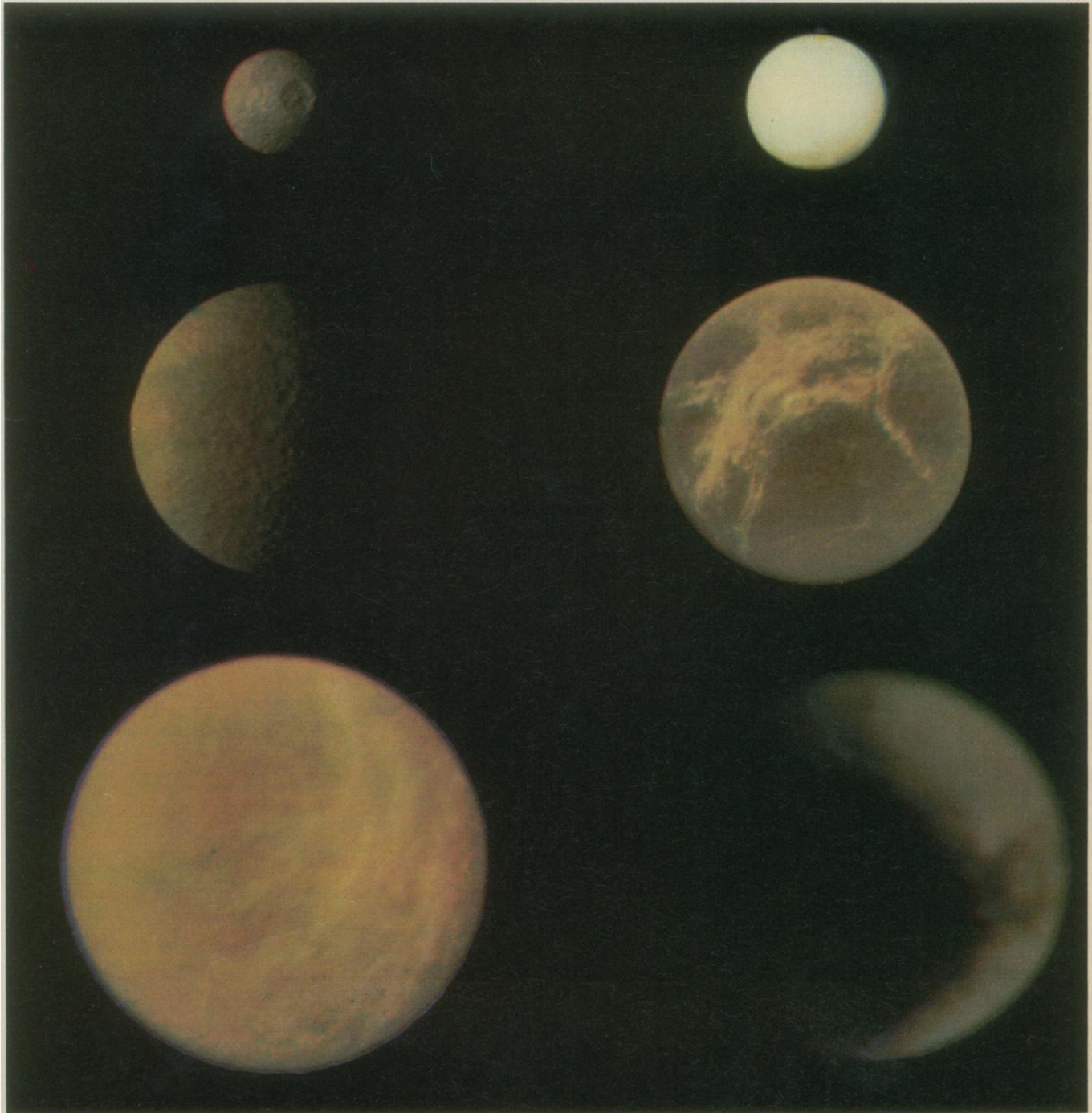
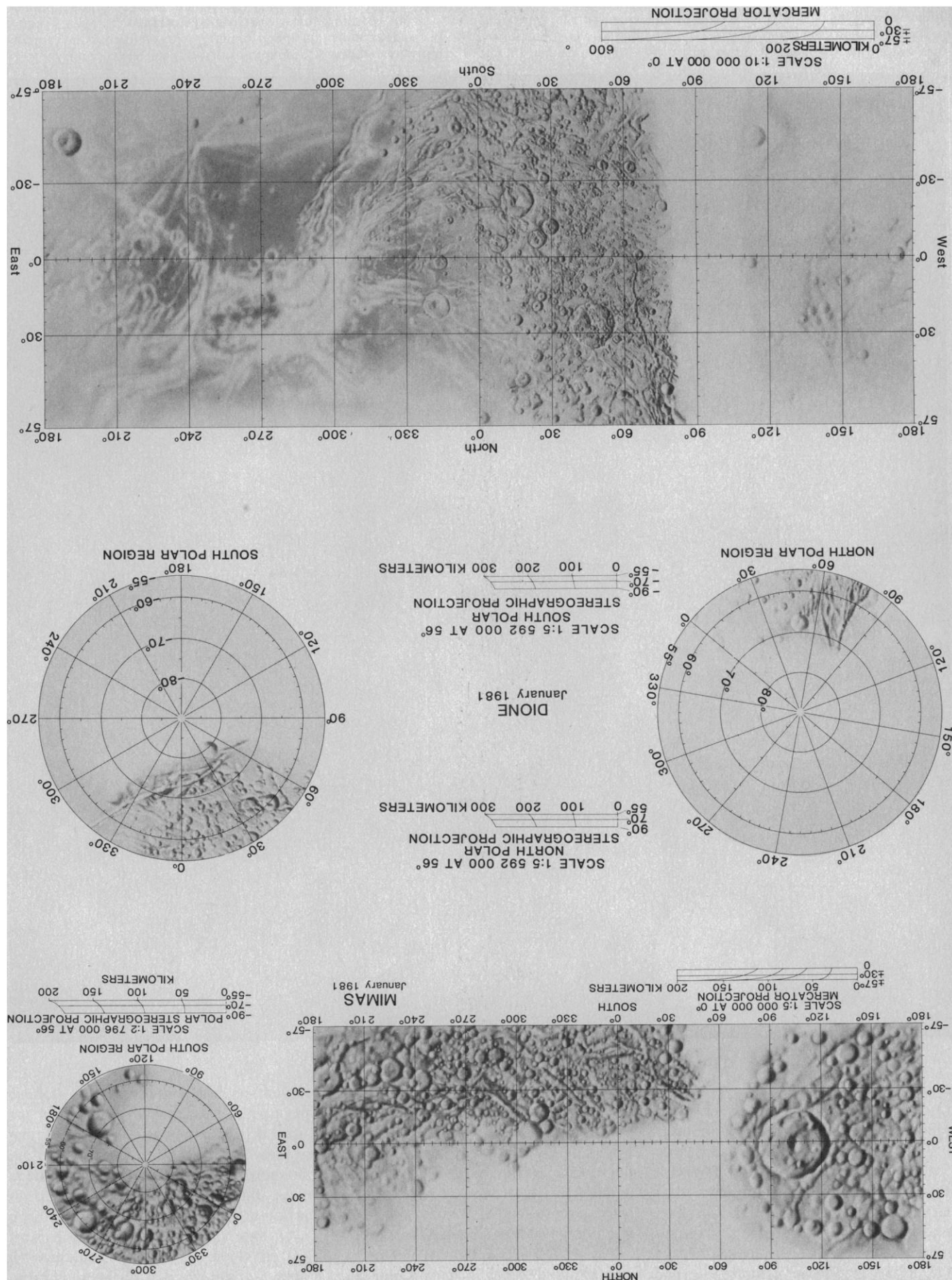
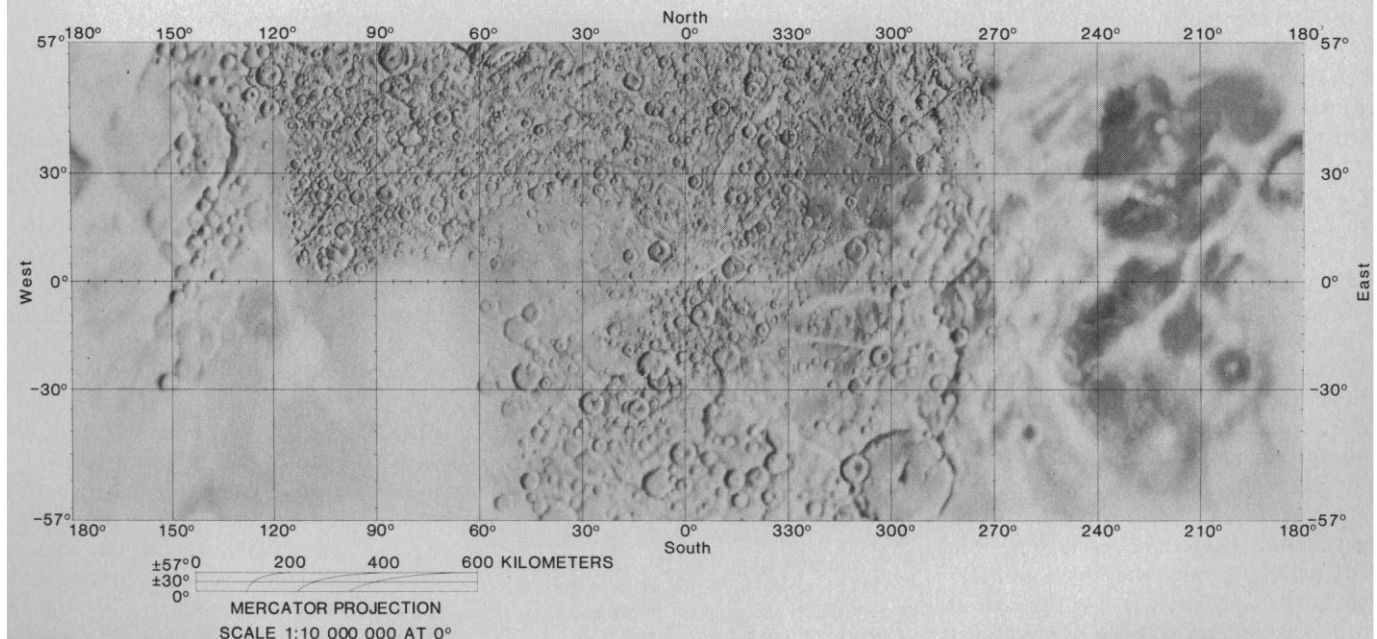
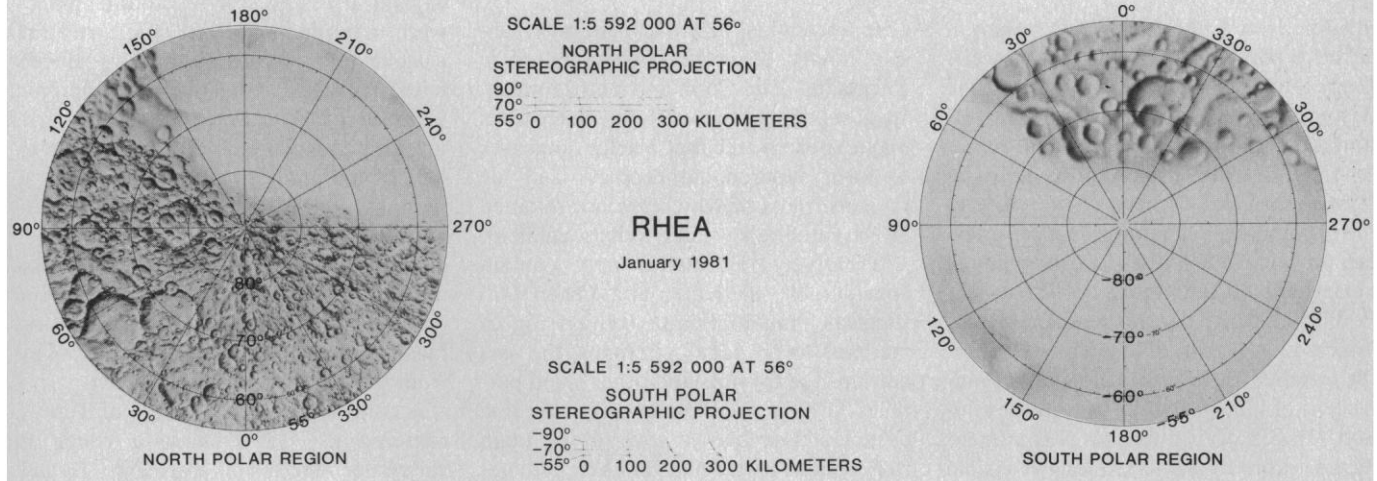
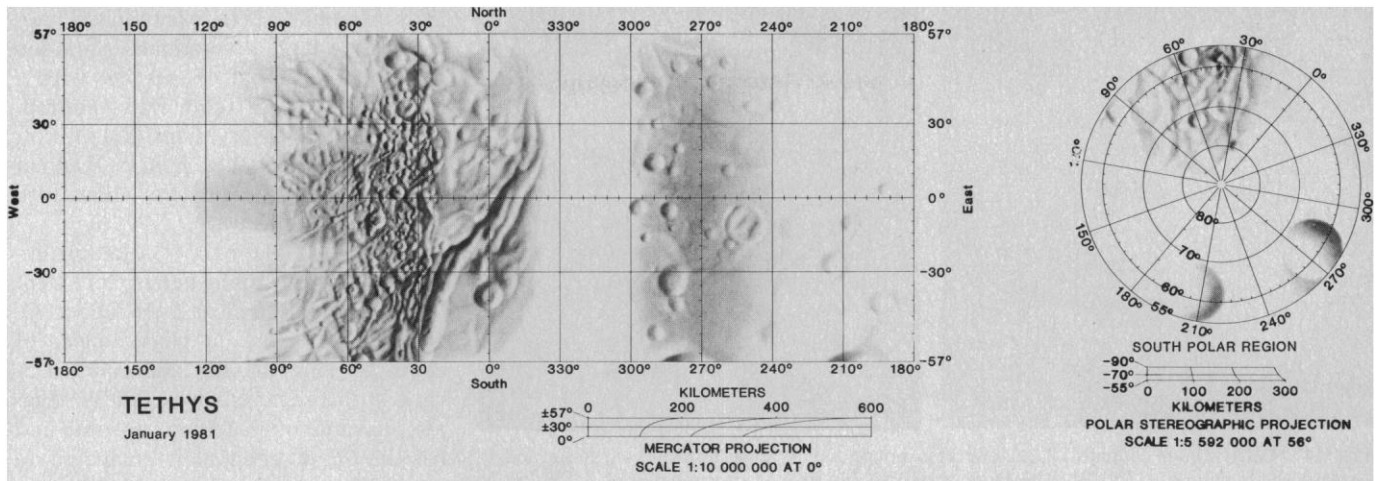


Fig. 12. Global color images of the six large icy satellites of Saturn (excluding Titan): Mimas, Enceladus, Tethys, Dione, Rhea, and Iapetus. Satellites are shown to scale. Relative albedo and color have been preserved qualitatively for comparison (with no compensation for differences in phase angle); geometric albedos range from  $\sim 0.05$  on the dark hemisphere of Iapetus to  $\sim 1.0$  on Enceladus. Phase angle, subspacecraft longitude, and resolution for the individual images are: Mimas ( $43^\circ$ ,  $22^\circ$ , 10 km/lp); Enceladus ( $14^\circ$ ,  $227^\circ$ , 12 km/lp); Tethys ( $72^\circ$ ,  $57^\circ$ , 11 km/lp); Dione ( $9^\circ$ ,  $270^\circ$ , 13 km/lp); Rhea ( $6^\circ$ ,  $313^\circ$ , 24 km/lp); and Iapetus ( $13^\circ$ ,  $19^\circ$ , 49 km/lp). [Montage prepared by J. A. Mosher, JPL Image Processing Laboratory]

Fig. 13. Preliminary maps of albedo and topography of Mimas, Dione, Tethys, and Rhea provided for orientation in discussions that follow. [Maps prepared by P. Bridges, J. Inge, H. Morgan, and F. Mullins under the direction of R. Batson]





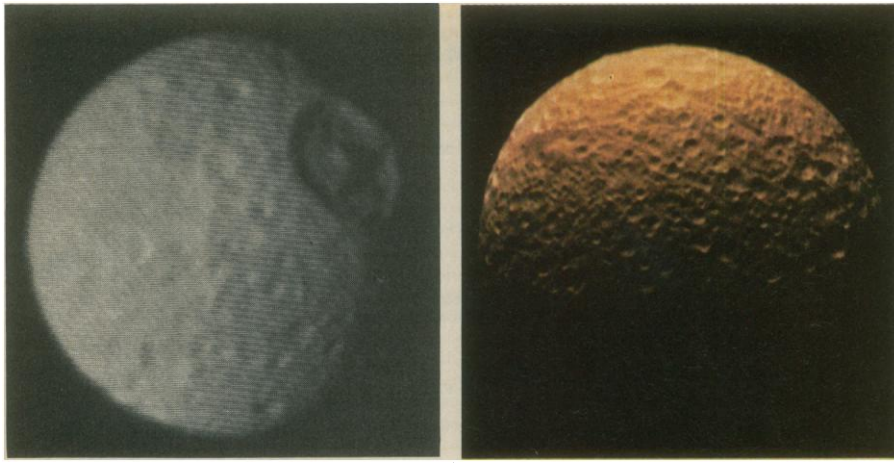


Fig. 14. (Left) Mimas' equatorial region. This image has a resolution of  $\sim 8$  km/lp and is centered at longitude  $\sim 150^\circ$ W. The large crater visible near the terminator is  $\sim 130$  km in diameter and has a central peak  $\sim 10$  km high. (Right) Mimas south polar region. This image is a color reconstruction with a resolution of  $\sim 2$  km/lp. A period of very heavy meteoritic bombardment is recorded on the surface. The small crater density on Mimas is even higher than that on the lunar uplands.

identified on Enceladus. This apparent absence may be due in part to the relatively low phase angles ( $12^\circ$  to  $15^\circ$ ) of the best images; even at these phase angles, however, craters with very high depth-to-diameter ratios, like those seen on Mimas, should have been visible close to the terminator. Thus, if craters are present on Enceladus, they must be much more subdued than those on Mimas.

With extreme contrast enhancement, intersecting bright bands can be seen at the terminator (Fig. 15), somewhat reminiscent of albedo features in low-resolution images of Europa. A sharp linear feature more than 150 km long is visible in some pictures, although whether it is a ridge, a trough, or simply an albedo marking cannot be determined. Some frames show brightening toward the limb.

In addition to its apparently smooth surface, Enceladus has a higher albedo than the other ice-covered satellites (Table 1). Detailed radiometric measurements from Voyager 1 images give  $I/F \sim 1.0$  at a phase angle of  $15^\circ$ . For a sphere to have a geometric albedo near unity, it must be more backscattering than a Lambert surface.

Enceladus' unusual surface properties may be related to recent resurfacing. Yoder (40) noted that Enceladus has an orbital eccentricity that is forced by Dione. This could result in significant tidal heating and could drastically alter the appearance of the surface, as on Europa and Io. The tidal action of Saturn on Enceladus may have kept most of the body liquid (water) under a very thin shell of ice, as suggested by Cook and Terrile (41). Saturn's E ring appears to exhibit a pronounced peak in brightness

near Enceladus' orbit (42) and may consist chiefly of particles escaped from Enceladus. The Cook and Terrile model suggests that punctures by meteoroids may expose water that briefly outgasses to form supercooled droplets and ice crystals, most of which are not retained by the satellite's weak gravitational field. Alternatively, Enceladus may contain considerable methane, and Owen (43) suggests that continuous outgassing of methane may occur. Perhaps the gas entrains ice crystals and other small particles, which then escape. The E ring particles then evolve toward the main ring system as a result of their interaction with Saturn's magnetosphere and associated plasma.

*Tethys.* Pre-Voyager data for Tethys

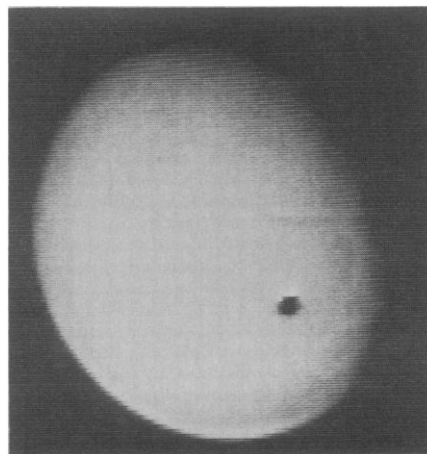


Fig. 15. Voyager 1 best view of Enceladus. This image of Saturn's second large icy satellite was acquired at a range of 625,000 km with a phase angle of  $15^\circ$ . The resolution ( $\sim 15$  km/lp) would be adequate to show large craters like those present on Mimas; they are evidently absent.

suggested that it is a low-density, ice- or frost-covered object. From limited photometric data, a rotational variation in brightness of about 15 percent with a minimum near  $270^\circ$ W was inferred. Ground-based observations (37) indicated an average visual geometric albedo of about 0.8 and a diameter of about 1000 km.

Two low-resolution ( $\sim 35$  km/lp) images of Tethys' trailing hemisphere were taken through the clear filter, about  $30^\circ$  of longitude apart, at phase angles of about  $10^\circ$  (Fig. 16, left and middle). A dark strip, centered at  $\sim 270^\circ$ W (Fig. 13), runs approximately north-south and has an  $I/F$  of about 0.6, compared to  $\sim 0.8$  for the brightest regions. Near the borders of the dark strip are circular markings, which are probably related to large impact craters like those visible in the highest resolution images (see Figs. 12 and 13). The low-resolution images were taken at low phase angle and the circular features are more likely albedo markings within craters than topographic expressions. The fact that these markings are conspicuous only near the borders of the dark strip suggests that stratigraphy controls their formation. Alternatively, as the dark area is centered near the antapex of motion, the markings may be due to impact "gardening" or dusting, or to coating by orbital debris on local slopes oriented toward or away from the apex of motion.

A contrast-enhanced image of Tethys centered at  $\sim 18^\circ$ W shows a trough or valley near the terminator (Figs. 13 and 16, right). Preliminary estimates of the trough's dimensions, assuming uniform albedo and a nominal photometric function (estimated error  $\sim 20$  percent), yield an average depth of  $\sim 3$  km, a maximum depth of 4 km, and a height of  $\sim 0.5$  km for its raised rim. Several ledges or terraces evident on the sides of the trough (Figs. 13 and 16, right) suggest a layered crust. A few large craters can be seen near the trough, but the resolution in this image is insufficient for an estimate of the crater population. Crater statistics on the highest resolution image of Tethys indicate that much of its surface has a dense population of deep craters, much like those on Mimas. The processes that produced the valley on Tethys are not clear, but some form of internal stress seems likely. Tethys' low density ( $\sim 1.0$  g cm $^{-3}$ ) suggests that it is nearly pure water ice; if so, it undergoes the greatest expansion on freezing of all the icy bodies. Voyager 2 will observe the same region (central longitude  $\sim 0^\circ$ ) at roughly ten times better resolution.

*Dione.* Dione is only slightly larger

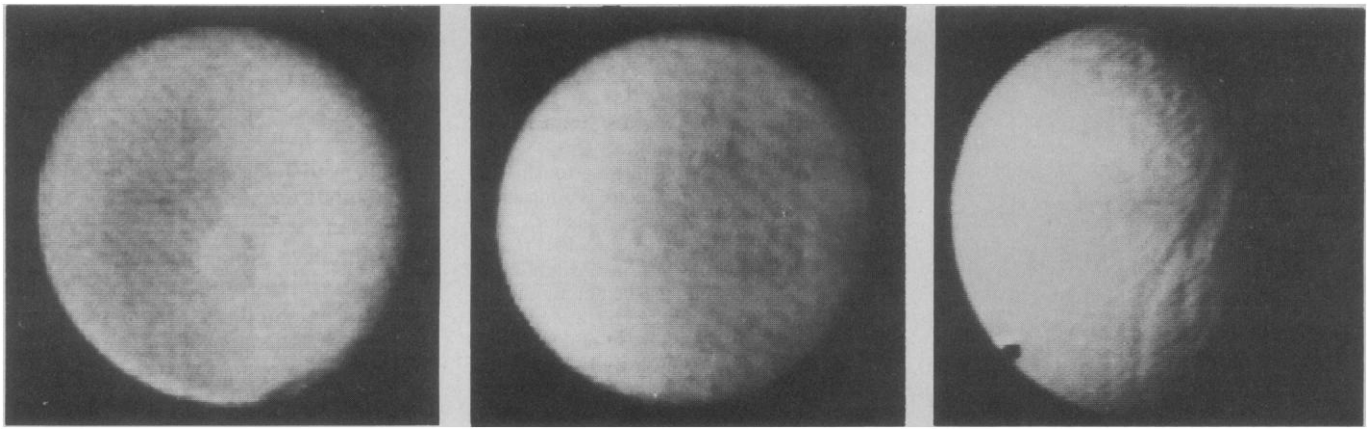


Fig. 16. Three views of the trailing hemisphere of Saturn's third icy moon, Tethys. (Left) Image centered at  $\sim 248^\circ\text{W}$ . (Middle) Image centered at  $\sim 279^\circ\text{W}$ . Both images have a resolution of  $\sim 35$  km/lp. A darker albedo feature centered at  $\sim 270^\circ\text{W}$  can be seen on both images, with circular albedo markings on both boundaries that are probably expressions of impact craters. (Right) Image taken at a range of 1,240,000 km and a phase angle of  $30^\circ$ , with a resolution of about 25 km/lp. An enormous valley about 1000 km long and 50 to 100 km wide runs from north to south along the terminator. Terraces inside this branching valley are faintly visible.

than Tethys but has a distinctly higher density (Table 1) and a different global appearance. For example, craters 10 to 50 km in diameter appear much deeper on Tethys than on Dione. Whereas Tethys shows only slight regional variations in its high average albedo, Dione shows large regional variations in albedo and also a complex network of bright wispy linear markings that divide the dark trailing hemisphere into polygons (Figs. 12 and 13). Dione exhibits some of the greatest albedo contrast in the Saturnian system, second only to that of Iapetus. The darker material on the trailing hemisphere has an  $I/F$  of about 0.3 to 0.35 at a phase angle of  $9^\circ$ , whereas the superimposed bright linear features have values between 0.5 and 0.6. The average brightness of the leading hemisphere is intermediate between these values.

Where they can be traced westward in relatively high-resolution images, the bright wispy markings are composed of, or pass into, a large number of relatively narrow bright lines (Figs. 12 and 17). Where these patterns can be traced into the highest resolution images (Fig. 18) of the bright hemisphere, in which the albedo contrast is not apparent, a few of the bright lines appear to be associated with narrow linear troughs and ridges that are extensions of the lines. Near the center of the complex of bright markings is an elliptical albedo feature about 240 km long ( $10^\circ\text{N}$ ,  $285^\circ\text{W}$ ; Fig. 13) that may be a large irregular crater or basin. If this feature is a crater, it is the largest one recognized on Dione. The bright markings do not form a pattern expected for rays; they may be controlled by a great regional system of fractures or faults associated with the putative basin. Fractures may also have been formed or reopened by internally generated stress-

es such as those associated with extension of the crust on freezing of the interior. The bright material, which is probably chiefly water ice or frost, evidently escaped from the interior of Dione along the fracture system—perhaps carried up by more volatile substances such as methane.

Like Mimas, Dione has a paucity of craters larger than about 30 km in diameter, but unlike Mimas it has a low overall crater population. The surface of the leading hemisphere (Fig. 18) consists of at least two terrains of contrasting topography. One, evidently older, is heavily cratered and has craters as much as 165 km in diameter; the other, which lies close to the leading meridian, is a less densely cratered plain. The crater populations of the two terrains are compared in Fig. 19. Few craters on the plain are larger than 40 km in diameter. Broad, low, northeast-trending ridges occur in the southern part of the plain (Figs. 13 and 18). The younger terrain has clearly

been resurfaced with a layer of material sufficiently thick to mantle preexisting cratered terrain. This could imply that an internal heat source has kept Dione active, generating an outpouring of material onto its surface over a sufficient time for its crater populations to vary markedly. Perhaps a relatively high concentration of radiogenic nuclides, which would be consistent with Dione's density, is responsible. Alternatively, the plains-forming event may have been an eruption of fluidized ice and rock, triggered by an impact or impacts. The fact that the plain occurs near the leading meridian suggests a high rate of bombardment; however, it would seem that the crater population on such a plain should be relatively high, contrary to what is observed.

Like the other icy satellites observed at close range, Dione is nearly devoid of ray craters. In the darker trailing hemisphere a faint but very extensive set of rays emanates from a bright spot (Fig.

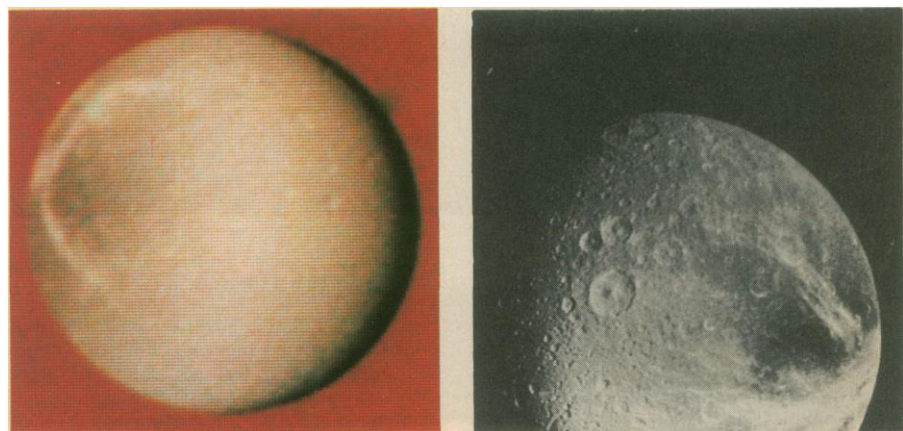


Fig. 17. Images of opposite hemispheres of Dione. (Left) The anti-Saturn side shows a generally darker trailing hemisphere that contains numerous bright streaks (7 km/lp). (Right) The Saturn-facing side, with the streaked trailing hemisphere to the right (4.5 km/lp).

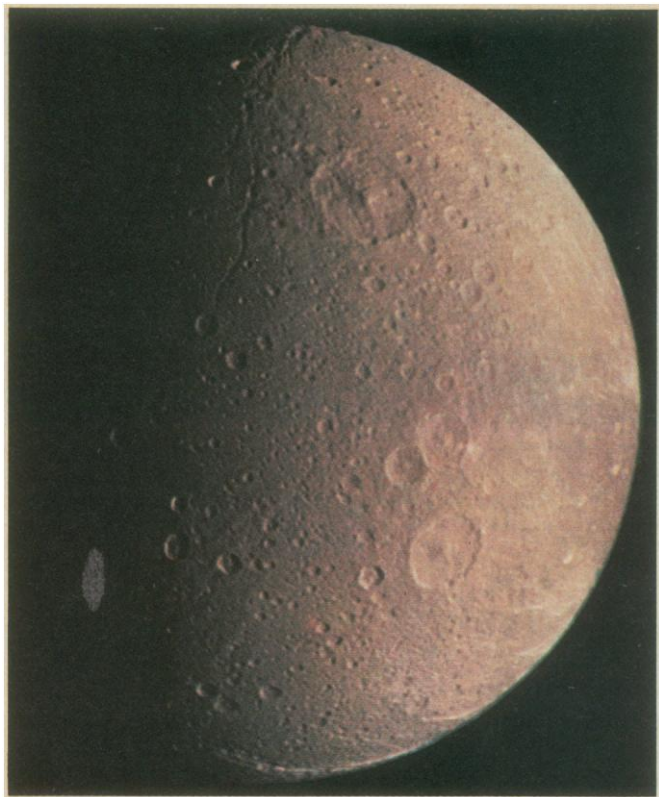


Fig. 18. Color view of Dione. This view of Saturn's fourth icy satellite is a mosaic of three color sequences. The resolution is  $\sim 3$  km/lp and the center of the image is at  $\sim 55^\circ$ W. Some of the light wispy streaks that are prominent on the trailing hemisphere can be seen at the limb to the right. At least one of the streaks near the terminator at the bottom is associated with a scarp. [Computer mosaic prepared by C. C. Avis, JPL Image Processing Laboratory]

12), which is presumed to be an unresolved crater. The apparent paucity of rayed craters on the icy satellites may be due to their generally high albedos, which would obscure fresh rays.

Other major topographic forms occur in the polar regions of Dione (Fig. 18). A long, linear valley, resembling a giant graben, extends for about 500 km across the south polar region. In the northern hemisphere a complex branching valley system, whose origin is under debate, extends from the polar region toward the equator. The presence, in the south, of a younger, sparsely cratered plain that has clearly undergone tectonic disruption and the complex, bright, polygonal albedo patterns, apparently developed on fractures, are evidence for a substantial period of crustal evolution and modification on Dione.

*Rhea.* Voyager 1 passed over the north polar region of Rhea at an altitude of only 59,000 km, providing our closest view of any of the icy satellites. Ground-based measurements had revealed a relatively featureless reflection spectrum in visible light, water-ice absorption bands in the near-infrared, a visual albedo of about 0.6, and rotational variations of 10 to 20 percent in full-disk brightness (37, 38).

As Voyager 1 approached Saturn, images of Rhea showed its global appearance to be highly variable with rotation. Figure 20 (left) shows the leading hemisphere to be relatively uniform and

bland, except for a large, diffuse, bright feature with radiating streaks. This presumed ray crater is centered in the leading hemisphere, near  $90^\circ$ W (Fig. 13), which was not observed at high resolution. The darker trailing hemisphere (Figs. 12 and 20, right) has bright wispy streaks similar to those seen on the trailing hemisphere of Dione. Unfortunately, as in the case of Dione, these markings were not in view during the near-encounter imaging sequence.

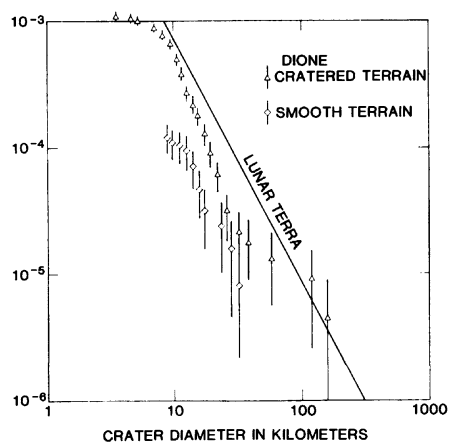


Fig. 19. Cumulative size-frequency distributions of presumed impact craters on Dione. The number of craters per unit area larger than a given diameter is plotted against that diameter. Error bars show statistical error of  $\pm \sqrt{N}$ , where  $N$  is the number counted. The cratered terrain is roughly in the center of the image shown in Fig. 17; the smooth terrain is along the terminator in Fig. 18.

The equatorial region that was viewed during close approach is about halfway between the first two views in Fig. 20, mostly in the bright leading hemisphere. Figure 21 shows a typical view of that region, which is dominated by impact craters and resembles the rolling cratered highland terra provinces of the moon and Mercury. Notably absent are the flattened crater forms common on the icy Galilean satellites, where some craters have lost nearly all topographic expression, presumably through viscous flow of the once-soft icy crusts. Evidently, Rhea's lower gravity and small diameter permitted rapid cooling and freezing and enabled its crust to support craters from an early period in its history. Rhea's large craters are irregular, often polygonal, suggesting that a rubble zone makes up the upper crust. Well-formed ejecta blankets are rarely seen around Rhea's large craters, another probable consequence of the lower gravity. Given the same ejection velocity as on the moon, crater ejecta on Rhea would spread out five times farther than lunar ejecta and would thus form a much thinner ejecta blanket. Curious bright patches are visible in some craters (Fig. 21) on both sun-facing and antisun-facing walls. They may be due to local frost deposits or, more likely, to continual exposure of fresh ice by impact gardening.

Bright and dark terrains (albedo contrast  $\sim 20$  percent) were observed at high resolution in Rhea's north polar region (Fig. 20, middle, and Fig. 22). The boundary between the terrains lies roughly along  $315^\circ$ . Large craters are much more abundant in the bright terrain. The abrupt nature of the boundary and the fact that the terrains are not symmetrically divided into leading and trailing hemispheres suggest that the difference in crater density is related to variation in surface age rather than in flux of impacting bodies; the flux should vary slowly with longitude from leading to trailing hemisphere. Perhaps the dark terrain was formed by extrusion of slightly darker material that buried pre-existing craters, and was then bombarded with bodies that virtually saturated it with small craters ( $\leq 50$  km in diameter). Evidently the production of large craters ( $\geq 50$  km in diameter) fell off dramatically before the resurfacing event. The evidence on Rhea strongly suggests two or more families of impacting bodies that were swept up at different times.

Observations of Rhea's equatorial region reveal a complicated surface evolution there as well. The central and upper right parts of Fig. 21 show a smooth plain with more muted topography than seen

in the lower left. The shaded relief map (Fig. 13) shows several regions of low crater density near the equator (300° to 330°W and 20° to 60°W). A complex network of narrow linear grooves and troughs occurs in the region from 290° to 330°W and 30° to 40°S; it ends abruptly on the west margin of an area containing large craters that appear mantled.

*Hyperion.* The best Voyager 1 image of Hyperion was obtained from a distance of  $4.6 \times 10^6$  km (84 km/lp) at a phase angle of 21°. In this image Hyperion is about seven picture elements across. (Voyager 2 will approach within half this distance.) From the Voyager 1 image, in which the subspacecraft longitude is 12°W, we derive a geometric albedo for the clear filter of 0.28, assuming a phase coefficient of 0.02 magnitude per degree (44). Combining this reflectance with a value of the visual magnitude of  $V(1,0) = 4.6$  gives 150 km for the radius. Direct measurement of the image yields a consistent value of  $150 \pm 10$  km for the radius. The new albedo value is considerably lower and the radius considerably larger than the values ( $\sim 0.5$  and  $112 \pm 5$  km, respectively) quoted by Cruikshank (37).

No direct data were obtained on the rotation state of Hyperion, but Peale (45) has argued that it should be in synchronous rotation with a period of 21.3 days. No Iapetus-like albedo differences are evident in the tiny Voyager image, and no systematic light variations have been found as the satellite orbits Saturn (46); albedo differences on the satellite are probably small. The near-infrared spectral signature of Hyperion seems to fall between those of Rhea and Oberon, which are known to have a significant component of water ice at their surfaces (37).

*Iapetus.* The best images of Iapetus were taken from a distance of  $2.5 \times 10^6$  km (49 km/lp). The radius of  $720 \pm 20$  km determined from these images agrees with the best ground-based value of  $724 \pm 60$  km (47). The most distinctive characteristic of Iapetus is the large albedo contrast between the trailing and leading hemispheres. Absolute visual magnitude ranges from 2.3 to 0.6, corresponding to average geometric albedos of  $0.49 \pm 0.05$  and  $0.10 \pm 0.01$  for the trailing and leading hemispheres, respectively. The boundary between the bright and dark hemispheres is meandering and gradational. On the Saturn-facing side it is at 340°W at the equator, angling over to 20°W at 40°N and 40°S (Fig. 12). The zone of gradation is 200 to 300 km wide and includes a dark ring (reflectance, 0.3) approximately 400 km in diameter

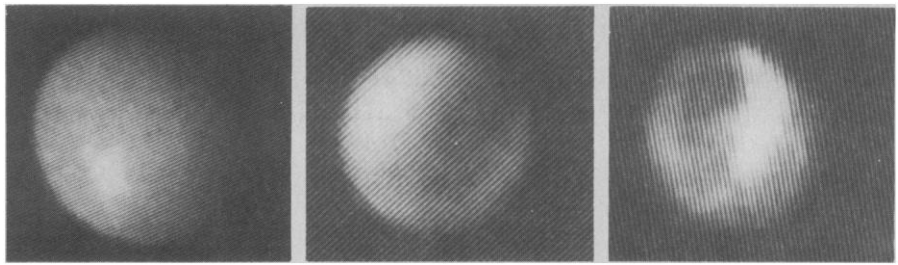


Fig. 20. Low-resolution views of Rhea, showing the satellite's changing global character with longitude. (Left) Image centered on  $\sim 85^\circ$ W, showing the relatively bland character of the leading hemisphere; the bright spot is probably due to a fresh impact. (Middle) Image centered on  $\sim 343^\circ$ W, showing the boundary between the leading and trailing hemispheres. (Right) Image centered on  $300^\circ$ W ( $\sim 144$  km/lp), showing light markings, which resemble the wispy markings on Dione when seen at higher resolution (Fig. 12).

that extends into the bright hemisphere. Several dark circular markings 50 to 200 km across lie farther out in the bright area. No bright markings can be seen on the dark hemisphere. The Voyager colorimetric data are consistent with ground-based data (37) suggesting that the surface of the bright hemisphere is predominantly water ice. On the side opposite Saturn, the boundary is also meandering and gradational over 200 to 300 km (Fig. 23). Another large ring occurs near this boundary, in this case on the dark hemisphere near the equator. Since this ring is readily seen at low phase angle, the pattern is probably due to albedo, not topography.

Iapetus' dark hemisphere is red, similar to the dark material of Callisto, and its albedo is consistent with that of car-

bonaceous chondrites. However, near-infrared measurements indicate a spectrum in the range 1.0 to  $3.0 \mu\text{m}$  that differs significantly from that of Callisto (48). There are several possible explanations for the dichotomy between the two hemispheres. Differentiation to produce ice-rich surface materials on one side and carbonaceous materials on the other is unlikely on both dynamical and geological grounds; it would result in hemispheres with different densities which would not align in the leading-trailing direction. The remaining explanations fall into two categories, involving exogenic or endogenic processes. Exogenic processes, which are attractive in explaining the leading-trailing dichotomy, include (i) water ice eroded off the leading hemisphere to expose darker rocks

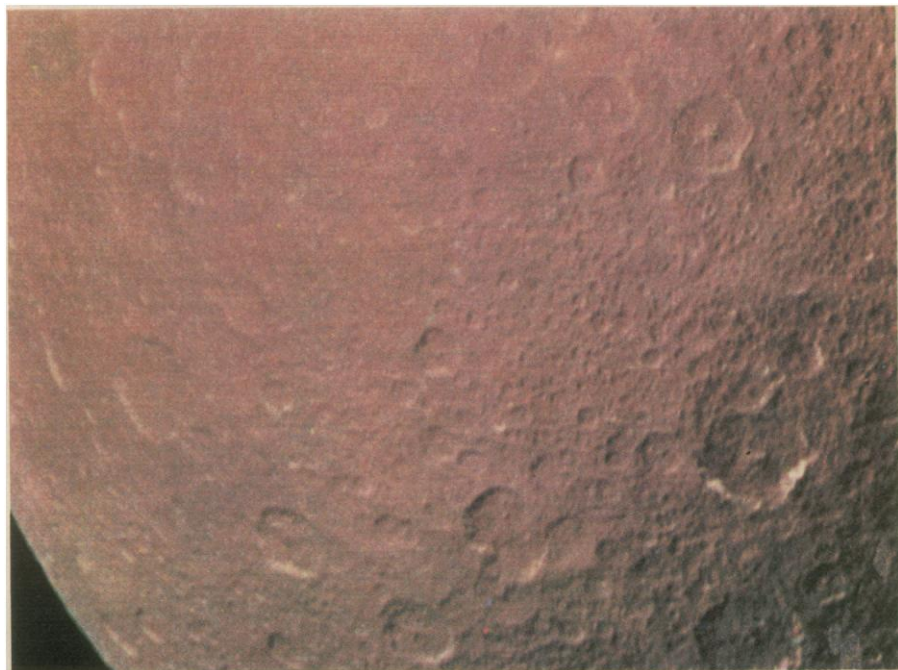


Fig. 21. High-resolution color image of Rhea. This composite shows a portion of Rhea's surface near the equator at  $\sim 15^\circ$ W. The images were taken just before closest approach of Voyager 1 to Rhea; they have a resolution of  $\sim 2.5$  km/lp and show an area of about 650 by 850 km. The average surface is quite bright ( $I/F = 0.5$  to  $0.6$ ), and even brighter areas are visible on the slopes of some craters, possibly due to fresh ice deposits or more likely fresh materials exposed by slumping.

Table 2. Long-period comet collision parameters and cratering rates to 10-km diameter for low-ice satellites of Saturn.

Parameter*	Mimas	Tethys	Dione	Rhea
$U$	1.50	1.55	1.57	1.60
$v_i$ (km sec <sup>-1</sup> )	25.3	22.3	21.1	19.9
$F$	14.1	10.1	8.7	7.3
$D$ (km)	90.9	73.4	66.4	62.5
$P_c$ (10 <sup>-13</sup> rev <sup>-1</sup> )	0.8	4.2	4.1	6.5
$\delta$	18.3	10.5	8.2	6.1
$\Gamma$ (10 <sup>-14</sup> km <sup>-2</sup> year <sup>-1</sup> )	0.51	0.30	0.17	0.12

\*Definitions:  $U$ , mean dimensionless encounter velocity at sphere of influence of Saturn, weighted by  $P_c$  ( $U$  = ratio of encounter velocity to Saturn's mean orbital velocity);  $v_i$ , mean impact velocity, weighted by  $P_c$ ;  $F$ , mean enhancement of flux of comets at orbital radius of satellite due to gravitational field of Saturn, weighted by  $P_c$ ;  $D$ , mean diameter of crater produced by impact of a 10<sup>16</sup> g cometary nucleus, weighted by  $P_c$ ;  $P_c$ , mean probability of collision of comet per perihelion passage;  $\delta$ , ratio of cratering rate at apex of satellite's orbital motion to cratering rate at antapex; and  $\Gamma$ , estimated rate of production of craters  $\geq 10$  km in diameter by impact of long-period comets.

beneath (49), and (ii) ice preferentially deposited on the trailing hemisphere (50). The boundary between the hemispheres is more abrupt, irregular, and complex than might be expected for infalling debris. An alternative endogenic process, suggested by the Voyager data, is extrusion of material from the interior. This could explain the boundary, with the large parted ring in Fig. 12 being a moat of dark material in a crater. Discrimination between these hypotheses may not be possible with the present

data. The Voyager 2 images will have 2.5 times better resolution.

*Cratering records and implications.* The impact crater populations on the icy satellites vary greatly both in number and in relative abundance of different sizes. Were the craters produced by debris orbiting Saturn, either remnants left over from the formation of the satellites and rings or fragments generated by large collisions within the system? Or were they produced by debris from outside the Saturn system, either early post-

accretional material in heliocentric orbits near Saturn or later long-lived cometary or asteroidal fragments?

Estimates of the impact flux from long-lived sources in the last 3 to 4 billion years suggest that the flux of cometary fragments is roughly 10<sup>4</sup> times that of asteroidal fragments. The contribution of long-period comets was extrapolated from their flux in the neighborhood of Earth, assuming that the perihelion distances are uniformly distributed between 1 AU and the orbit of Saturn (51). Collision probabilities, velocities of impact, masses of comet nuclei, and cratering rates (Table 2) were estimated as described by Shoemaker and Wolfe (51).

Two trends are indicated by the model calculations for cometary debris (Table 2). First, the mean impact velocities and therefore crater production rates increase inward from Rhea to Mimas, due largely to gravitational acceleration by Saturn. Second, the cratering rates at the apex and antapex of motion (leading and trailing hemispheres) differ, ranging from about 20:1 for Mimas to more than 5:1 for Rhea. These trends generally apply for all external sources (such as short-period comets or asteroids in heliocentric orbits), although long-period comets have slightly higher impact rates due to their higher velocities.

In addition to long-period comets, there may be about 10<sup>4</sup> comet nuclei of diameter  $> 1$  km that have been captured in relatively short-period orbits by repeated encounters with Saturn. As most of these bodies would be too far from the sun to show detectable cometary activity, their existence is inferred almost entirely from dynamical arguments; Chiron is the only apparent member of this "Saturn family" of comet nuclei so far discovered. A set of plausible orbits for Saturn-family comets suggests that their cratering contributions would be somewhat greater than those of long-period comets given in Table 2. The equivalent cratering rate for the moon for craters 10 km and larger is about  $2 \times 10^{-14}$  km<sup>-2</sup> year<sup>-1</sup>.

Including Saturn-family comets, our best estimate for Rhea is a cratering rate by external debris about a factor of 7 lower than that for the moon; our estimate for Mimas is about the same as that for the moon. We tentatively conclude that the cratering rates of debris coming from outside Saturn's system over the last 3 to 4 billion years (i) increase systematically inward from Rhea to Mimas, (ii) differ greatly from leading to trailing hemispheres (by factors of 5 to 20), and (iii) are generally lower than lunar rates.

We now examine the observed crater

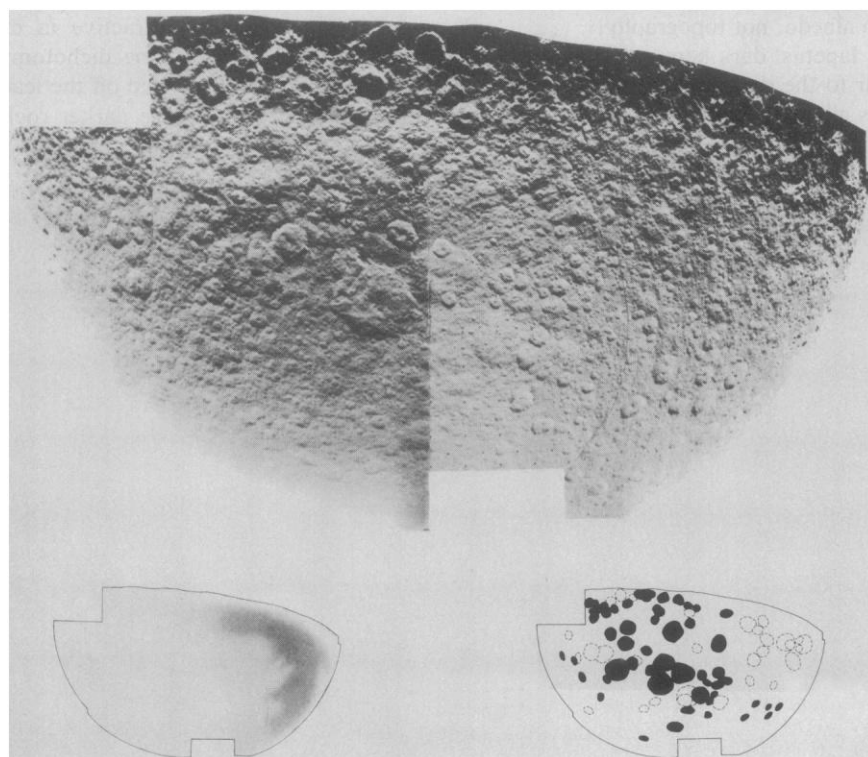


Fig. 22. Rhea north polar mosaic. During the close encounter with the largest inner icy satellite, special image motion compensation was used to acquire this mosaic of Rhea's north polar region. The resolution is about 1 km/lp. The images have been high-pass filtered to enhance details of the topography. The low-resolution inset (lower left) is a polar projection airbrush sketch of the approach images (Fig. 20), showing the boundary between bright and dark terrains in the north polar region. The second inset is a sketch of large craters in the polar region mapped on the mosaic. Craters that appear fresh and superposed on the surface are black; apparent mantled craters, faintly visible, are shown as circles. Notice the strong correlation between dark terrain and the absence of large craters.

populations for these characteristics. Smoothed, average crater size-frequency distributions for Mimas, Dione, and Rhea are shown in Fig. 24. The curve for Mimas represents craters measured on the three highest resolution images. Dione's curve represents the cratered plains and heavily cratered terrain, but is dominated by the plains. Rhea's curve is dominated by the bright leading hemisphere. Comparison of the three distributions suggests that at least two different crater populations are involved. Population I is characterized by a relatively high abundance of craters larger than  $\sim 20$  km. Population II is characterized by abundant craters smaller than  $\sim 20$  km and a general absence of larger craters. Although the curves for Dione and Mimas are dominated by population II, the most heavily cratered terrains on Dione and Rhea preserve a record of population I. The youngest cratered plain observed on the three bodies, located near the terminator on Dione (Fig. 18), is imprinted by population II. On Dione, population II postdates population I, as it also appears to on the bright and dark terrains in the north polar region of Rhea.

Regions on Rhea and Dione that display population I craters date back to a very early period of postaccretional bombardment, as do the highlands of the moon, Mars, and Mercury and the heavily cratered terrains on Ganymede and Callisto. As for the moon, an extremely high flux and rapid decline around 4 billion years ago is implied. Whether population I is due to debris in heliocentric orbits or to fragments coorbiting with the satellites during this early period cannot be determined.

In regard to population II, a first impression is that the higher average crater density for Mimas than for Dione might be evidence for cratering by extra-Saturnian debris during the last 4 billion years. Other observations, however, suggest that population II craters were generated by debris indigenous to the Saturn system. Compared to the lunar maria, the abundance of the population II craters ranges from a factor of 2 or 3 times higher for Dione's plains to a factor of more than 100 times higher for Mimas and Rhea. Since the estimated modern cratering rates are lower on the Saturnian satellites than on the moon, the population II craters on Rhea and Mimas could not have been produced under modern rates during the last few billion years. Such a strong statement cannot be made for Dione, as our calculations could be in error by a factor of 10. The distribution of craters on Dione, howev-

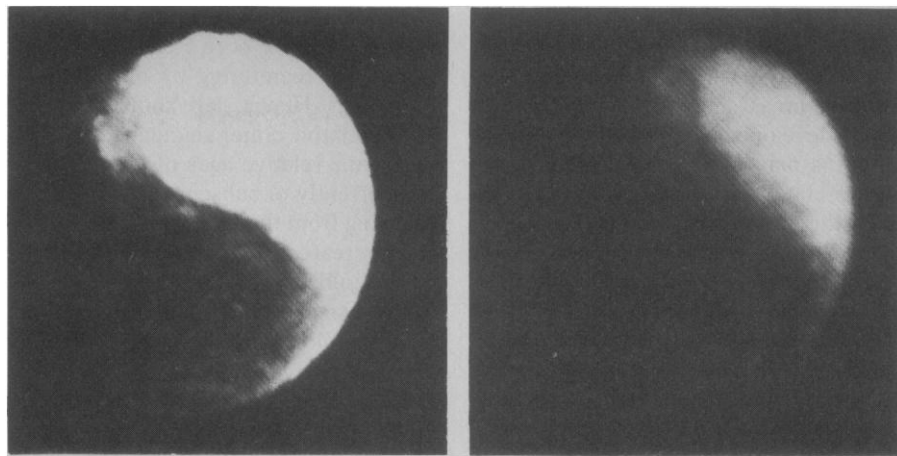


Fig. 23. Image of Saturn's large icy satellite, Iapetus. This view was taken at a range of  $2.5 \times 10^6$  km and a phase angle of  $41^\circ$ . The resolution is about 50 km/lp; the central longitude is  $45^\circ$ W. Two versions are shown: (left) enhanced to show the regional boundaries in albedo patterns, and (right) enhanced to show an impact crater with raised rim and central peak near the terminator in the overlap between bright and dark regions.

er, does not follow the leading-trailing variation expected for an extra-Saturnian source; in fact, the least cratered plains are in the leading hemisphere. We conclude that population II craters are produced from debris indigenous to the Saturn system.

Elsewhere in the solar system, secondary craters produced by large primary impacts have common characteristics. The largest secondary is typically an order of magnitude smaller than the primary, and the cumulative number of secondaries increases rapidly with decreasing diameter, roughly as the inverse third or fourth power of diameter. Hence such secondary populations have steep size-frequency distributions and no craters larger than a certain diameter. Saturn's population II craters share these attributes. Most of the secondary fragments ejected from the large primary impact crater on Mimas would escape; the escape velocity from Mimas is only  $0.16 \text{ km sec}^{-1}$ . Thus each primary impact would eject debris into independent orbit about Saturn. Most of these orbits would have semimajor axes similar to that of Mimas because the escape velocity of Mimas is small compared to its orbital speed. Therefore the debris would soon be swept up again, producing a large number of low-velocity secondary craters.

On the moon, the size-frequency distribution of secondaries around a large primary reflects the distribution of kinetic energies of the ejected fragments. As on the moon, fragments ejected from the surface of an icy satellite will collide with that surface with the same average energy they had when they left. Hence the returning fragments will impact with an energy distribution similar to that on the

moon. Leaving aside rheological properties and effects of gravity on excavation, the secondary craters will be of similar size. In summary, the characteristics of population II most resemble those expected for large impacts by debris within the system.

If populations I and II are not related to long-term cratering by extra-Saturnian debris, does evidence for such cratering exist? The global views of Dione (Fig. 17) show the leading hemisphere to be bland and bright and the trailing hemisphere to display complex albedo patterns. The transition is regular in angular distance from the apex ( $90^\circ$ W). The shaded relief map (Fig. 13) shows the complex albedo pattern centered in the trailing hemisphere at  $270^\circ$ W. We suggest that this appearance is due to a higher rate of impact gardening by extra-Saturnian debris on the leading than on the trailing hemisphere ( $\sim 10:1$ ). The craters responsible for the gardening are simply too small to be detected with the Voyager 1 resolution. Also, the change in flux with angular distance from the apex is not gradual but occurs abruptly in the trailing hemisphere. The ratio of flux between the apex and  $90^\circ$  from the apex is only 2:1, but from there to the antapex the ratio is 5:1. This is consistent with the abrupt transition from the region of bright uniform albedo to that of complex albedo in Fig. 17. Rhea shows the same effect; the complex albedo patterns in Figs. 12 and 20, right, are in the trailing hemisphere. Figure 20, middle, shows the transition from this region to the bright leading hemisphere, which is bland except for the bright ray crater.

We conclude that the albedo patterns on Dione and Rhea have been preserved

in the more protected, trailing hemispheres and that these satellites were once covered with these complex patterns. Mimas and Tethys may never have developed such patterns, or the patterns may have been erased. If our interpretation of these patterns is correct, the best records of the early histories of the satellites are hidden on the trailing hemispheres. Figure 17, right, shows that the bright markings in Dione's trailing hemisphere are younger than the large craters on the dark terrain. Evidently the plains-producing activity lasted for some time after the bombardments that formed population I and possibly population II.

These observations suggest the following general model for the geologic histories of the icy satellites. After accretion they were intensely bombarded by objects that produced the craters of population I, dominated by craters 20 to 100 km in diameter. Population I cratering then ceased as the source was rapidly depleted. Subsequently, regions on Dione and Rhea were resurfaced with plains materials that obliterated population I craters. Collisions by late-arriving debris or fragments within Saturn's system produced numerous secondary fragments that created the population II craters on top of

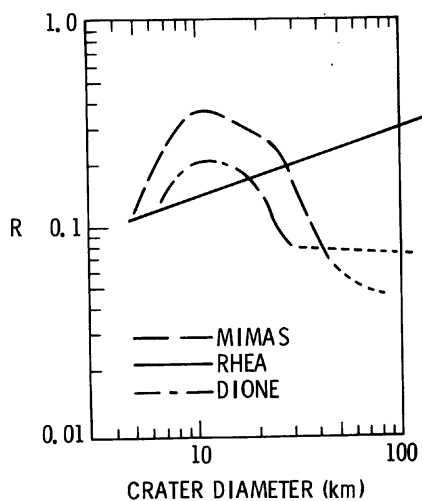


Fig. 24. Comparison of average crater populations on Mimas, Dione, and Rhea. Although Dione and Rhea show variability in crater populations from region to region, the average populations are substantially different. Shown here are the populations on the three bodies relative to a distribution  $N D^{-2}$  (where  $N$  is the number of craters per unit area larger than diameter  $D$ ), which would be represented by a horizontal line in this plot. The level is proportional to the number density. On the average, Mimas and Dione are highly deficient in craters larger than about 10 km relative to the average for Rhea. The different relative abundances of large and small craters suggest different populations of impacting bodies and variations in surface age on and among the satellites.

these plains. The population I craters on Mimas may have been erased principally by intense recratering by population II projectiles. Hence, care should be taken to use relative crater abundances in comparing the relative ages of the satellites. Concurrently or subsequently, materials escaping from the interiors of Dione and Rhea created a complex network of bright albedo patterns. Mimas and Tethys, smaller and less dense, may not have developed the endogenic activity necessary to produce dark plains and bright streaks. Finally, over the last few billion years, gardening by extra-Saturnian debris has gradually erased the bright and dark patterns on the leading hemispheres of Dione and Rhea; the patterns remain in the more protected regions of their trailing hemispheres.

*Implications of observed densities of satellites.* The Saturnian satellites differ in several important respects from the Jovian satellites. First, with the exception of Titan, they are smaller than the Galilean satellites. Second, as suspected before Voyager, they have lower densities than the Jovian satellites (Table 1). Third, although some pre-Voyager models suggested that the density of the satellites would increase with proximity to the primary (52), as is the case in the Jovian system, it now appears that the reverse is true: in general, density increases from Mimas to Titan.

Figure 25A is a plot of radius versus density for the icy satellites. Also represented are two theoretical models from Lupu and Lewis (53) showing the effects of self-compression in the larger satellites. Note that Ganymede, Callisto, and Titan all fall above the curve for a 40 percent mass fraction of "rock" (assumed to have a density of  $3.7 \text{ g cm}^{-3}$ ), whereas the other well-determined Saturnian satellites fall on or below it; the density of Tethys is close to the curve for a pure ice model. These data suggest that Titan's composition is close to that of Ganymede or Callisto (if the major condensed volatile is water) and that the other satellites have less rock-rich compositions. Figure 25B gives the result of a computation of the limits on total rock mass fraction in the satellites, taking the extremes of the density errors and assuming a density of either  $2.2 \text{ g cm}^{-3}$  (C1-type meteoritic) for the rock fraction and  $0.939 \text{ g cm}^{-3}$  for uncompressed water ice. Even with these uncertainties, Tethys must have a lower rock fraction than the other satellites and Mimas an intermediate one. The general trend of increasing density toward the outer part of the system probably reflects the con-

ditions during satellite formation. Deviations from the trend may reflect variations in composition and density of the fragments that coalesced to form the satellites.

It may be significant that the denser members of the system show far more evidence of internal activity at some stage in their histories than do the less dense ones. For example, Tethys and Dione have very different appearances despite their nearly identical sizes. Greater amounts of rocky material, implying larger proportions of heat-producing radionuclides, may be more important than size in determining the thermal evolution of bodies of this general size.

Detailed calculations of the gravitational contraction of these systems (46) suggest that Jupiter and Saturn were initially several hundred times their present size; they then slowly contracted, underwent rapid hydrodynamic collapse to a size several times their present dimensions, and finally resumed slow contraction. The disk of gas and dust that gave rise to the satellites and rings may

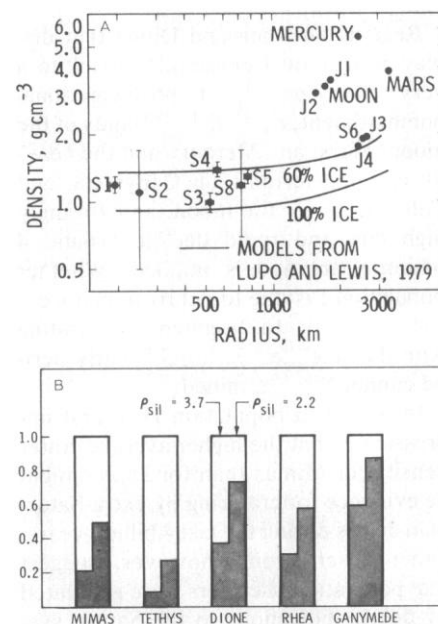


Fig. 25. Comparison of sizes and densities of the icy Saturnian satellites. (A) Best estimates of the densities of the satellites with Voyager 1 data included (see Table 1). The large error bars for Enceladus (S2) and Iapetus (S8) are due to poor knowledge of their masses. (Voyager 2 will improve the mass determination for Enceladus.) The Tethys (S3) and Dione (S4) pair, which have very similar diameters, are at the extremes of density ( $1.0$  and  $1.45 \text{ g cm}^{-3}$ ) for the satellites. (B) Mass fractions of rock and ice consistent with the densities of the Saturnian satellites compared with Ganymede. Two cases are shown: ice and rock with a density of  $3.7 \text{ g cm}^{-3}$  (typical for mantle rocks, the moon, and Io) and ice and rock with a density of  $2.2 \text{ g cm}^{-3}$  (typical for material like carbonaceous chondrites).

have formed during the early collapse phase. The intrinsic luminosities of the two planets may have been several orders of magnitude larger during the period of satellite formation and declined monotonically with time to their present values. If so, the temperature conditions within the circumplanetary nebulae were dominated by the planetary heat fluxes.

It has been suggested (54) that the intrinsic luminosity of Jupiter was so high during satellite formation that water vapor was unable to condense in the inner region of the Jovian nebula. This would explain why Io and Europa have mean densities typical of objects made mostly of rock, whereas Ganymede and Callisto appear to have a water ice component close to that predicted for condensation from a nebula of solar composition. Because Saturn is about a factor of 3 less massive than Jupiter, its intrinsic luminosity may have been a factor of 10 smaller than that of Jupiter (55). During the period of satellite formation, water vapor within Saturn's nebula could condense much closer to the planet (56). This is consistent with the observed mean densities of Saturn's satellites, all of which are in the range of 1 to 2 g cm<sup>-3</sup>.

Further, during satellite formation Saturn may have extended to about five times its present size, to just beyond the present orbit of Tethys (55, 56). In that case silicate grains would have been largely removed by gas drag from the innermost satellites, but would have remained in the vicinity of Dione, Rhea, and Titan. Thus satellites and rings that formed within the initial radius of Saturn may have had a smaller amount of rocky material available.

This model provides only a tentative explanation of the trend of increasing density away from Saturn. It does not explain the random deviations, nor the lower density of Tethys compared to Mimas or of Rhea compared to Dione. To account for these apparent anomalies, we speculate that these icy bodies are so small that the stochastic character of accretion itself may be recorded in their bulk properties. If the planetesimals—the lumps of matter accumulating in the final stages of accretion—were heterogeneous in their bulk properties, then random factors would control the final makeup of small bodies. By chance, Dione and Mimas may have gathered a few more rocky planetesimals than did Tethys and Rhea. If so, we have found a class of objects in the solar system that reflect the character of accretion itself.

**Small inner satellites.** Five small satellites are now known within the orbit of Mimas. The two outermost, discovered

by Dollfus (57) and Fountain and Larson (58), are in orbits separated by only 50 km; they are sometimes referred to as the coorbital satellites and are designated here as 1980S1 and 1980S3. Their irregular shape (Figs. 27 and 29) and their orbits are consistent with their having once been a single body that was split by an impact more severe than that which caused the large crater on Mimas. Three satellites that orbit closer to Saturn than these have been discovered by Voyager 1 (59, 60); they are designated, in order of discovery, as 1980S26, 1980S27, and 1980S28. Later, they will be given permanent names by the International Astronomical Union (61). The larger two (1980S26 and 1980S27) bracket the F ring and establish its stability or

instability. The smallest of all known Saturnian satellites, 1980S28, orbits just outside the A ring and seems to establish the outer boundary of the entire broad ring system (Fig. 26). The orbital parameters of these satellites are discussed by Synnott *et al.* (62).

By a coincidence of illumination and viewing geometry, Voyager 1 obtained six images of the trailing coorbital satellite (1980S3) at a time when the penumbral shadow of the F ring was crossing the satellite from south to north (Figs. 28 and 29). Analysis of the shadow's photometry and shape should give an indication of the optical thickness of the F ring and some topographic contours of the satellite itself.

The leading coorbital satellite, 1980S1,



Fig. 26. (Left) 1980S28 orbiting between the F ring and the A ring. (Right) The satellite's oblong shape.

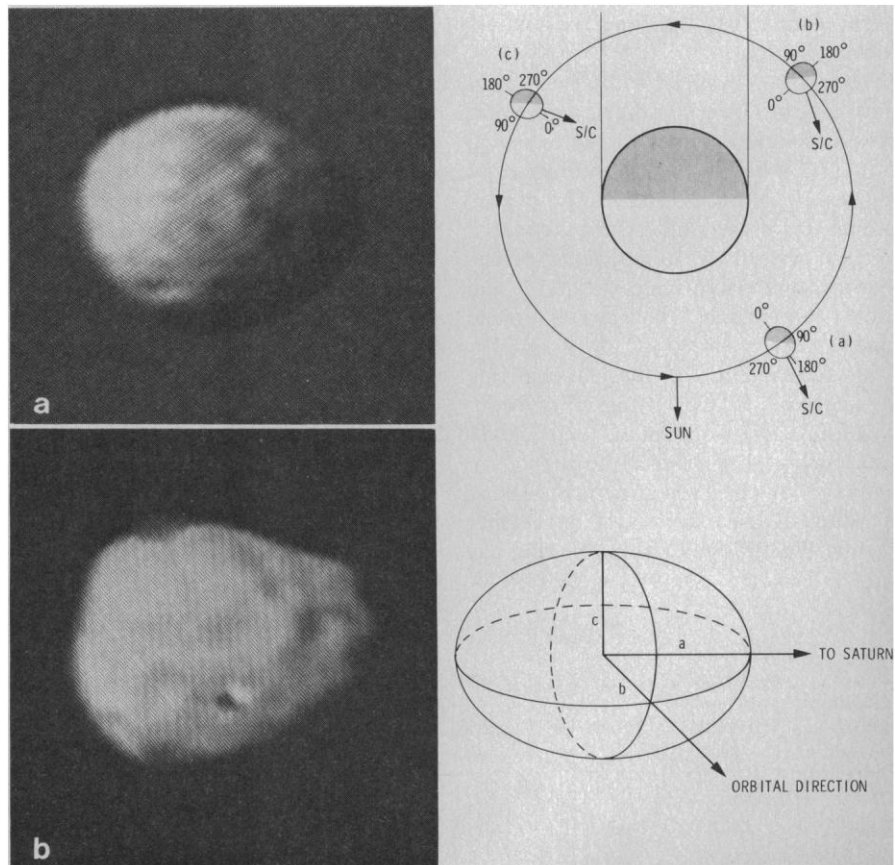


Fig. 27. (Left) 1980S1 at (a) range 611,000 km, resolution 11.3 km/lp, and phase angle 27.5°, and (b) range 521,785 km, resolution 9.65 km/lp, and phase angle 25.1°. The image shuttered in viewing geometry (c) was badly smeared. (Top right) Viewing geometry as seen from Saturn's north pole; arrows indicate the direction of the spacecraft (S/C); the shaded area represents the nightside. (Bottom right) Standard definition of axes of triaxial ellipsoid.

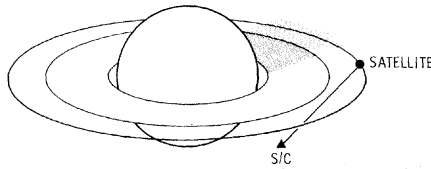


Fig. 28. 1980S3, the trailing coorbital satellite, seen by the spacecraft (S/C) from 45° below the satellite's equatorial plane.

was observed at phase angles 25°, 27°, and 73°. Average  $I/F$  values at these phase angles are 0.27, 0.31, and 0.12. Although these data do not define a detailed phase function, they are not unreasonable for a bright object. The equivalent linear phase coefficient would be  $\sim 0.02$  magnitude per degree, although this may not be valid for high phase angles. The trailing coorbital satellite, 1980S3, has an average  $I/F$  of 0.15 at phase angle 57°. If the leading and trailing satellites have the same phase function, they will both be about the same brightness at 0° phase ( $I/F \sim 0.4$ ). Approximate albedos of 0.08 and 0.25 have been measured for 1980S27 and 1980S28 at phase angles of 12° and 40°, respectively. Currently known properties of these small inner satellites are listed in Table 3. In the three cases where relevant data exist, the long axis points toward Saturn.

*The rings.* Voyager 1's observations of Saturn's rings reveal a much more complex and varied structure than expected from Earth-based photos or Pioneer 11 images (4). Here we discuss the overall properties of the rings seen in Voyager images: the major components of the system, their large-scale structure, and gross comparisons that can be made among them.

As seen in Fig. 30, the classical ring elements (A, B, C, D, Cassini division, and Encke division) retain their significance in that they differ in the qualitative nature of the observed structure. Closest to Saturn is the extremely faint D ring, seen in Fig. 31. Material in this ring has

been detected at a radial distance of about 66,500 km from the planet center, but it could extend down to Saturn's atmosphere; its outer edge is the inner edge of the C ring. The D ring consists of numerous narrow features that vary in width from several hundred kilometers to the resolution limit of 35 km. These features were observed in both forward and back scattering, indicating a negligible component of small (micrometer-sized) particles. The optical depth is extremely small and it is very likely, despite reports to the contrary (63), that the D ring has never been observed from the ground.

The C ring consists of broad bands of optically thin regions, giving it a transparent appearance in transmitted light (Fig. 32). Within these transparent regions are many optically thick ringlets, at least one of which is an eccentric feature (see Fig. 33).

The B ring is the largest component of the ring system, extending over 25,000 km, and is in general the brightest and most optically thick. At small phase angles the B ring exhibits modest structure; at large phase angles it resolves into hundreds of bright ringlets and dark gaps, with widths from 100 km down to the limit of resolution. Over most of the B ring, little or no large-scale (several hundred kilometer) systematic spacing of ringlets is evident. When seen in diffuse transmission, many of the narrow features in the ring appear relatively transparent. No evidence for such narrow, randomly distributed, optically thin regions exists outside the B ring. The boundary between the B and C rings is sharp ( $\sim 10$  km) and is bordered outward by a 600- to 800-km-wide region of extremely large optical depth, with no evidence of narrow gaps.

The next classical feature, at a radius of approximately  $118 \times 10^3$  km, is the Cassini division, which until recently was believed to be a single gap. Voyager 1 high-resolution images (Fig. 34) reveal a wealth of detail: five broad, sharp-

Table 4. Ring optical depths and albedos.

Ring	Radial zone	Optical depth	Single scattering albedo*
A	Central half	$0.4 \pm 0.08$	$0.63 \pm 0.08$
B	Inner third	$>1^\dagger$	$0.63 \pm 0.08$
C	Central half	$0.1 \pm 0.02$	$0.21 \pm 0.05$
Cassini	Four inner bands	$0.08 \pm 0.02$ $0.07 \pm 0.02$ $0.07 \pm 0.02$ $0.10 \pm 0.02$	$0.32 \pm 0.05$

\*Lambert spheres are assumed to represent the particle phase function.  $^\dagger$ The effective B ring optical depth is ill-determined due to the existence of narrow regions of very low optical depths within an overall highly opaque layer.

edged, evenly spaced bands, each of which exhibits structure down to the limit of resolution. The arrangement of large- and small-scale features in the Cassini division, as well as in the C ring, shows a regularity that at present cannot be attributed to resonances with known satellites. The optical density of the bands is similar to that of features in the C ring. This similarity is paralleled in the photometric properties of these two ring elements, which are notably different from those of the A or B ring (see Fig. 30).

The A ring and the Encke division within it are the last major features of the classical ring system. Although in comparison with the other components the A ring is devoid of spectacular detail, high-resolution images show many narrow and well-ordered features that may be associated with satellite resonances. The reported azimuthal asymmetry in A ring brightness has been confirmed in low-resolution Voyager images. The Encke division is not entirely free of material but contains at least two very narrow, clumpy ringlets.

Beyond the outer edge of the A ring there are several more features. The F ring, discovered by Pioneer 11 (4), is found to be far more complicated than was imagined. This ring lies between the orbits of 1980S27 and 1980S26 at a radius of about 140,000 km. It will be discussed later.

Still farther out is the G ring at a radius of about 170,000 km. It can be seen in Fig. 31 as a thin line across the frame. Image smear has broadened the ring's appearance; however, the ring seems to be very faint and very narrow. Charged particle experiments on Pioneer 11 (60) indicated the presence of material at this radius.

Figure 31 also shows the E ring in forward-scattered light. This ring is extremely optically thin and extends from

Table 3. Small inner satellites.

IAU satellite designation	Mean orbital radius (km)	Orbital period	Observational resolution* (km/lp)	Phase angle (deg)	Mean radius (km)	Ellipsoidal axes (km)		
						A	B	C
1980S1	$1.51472 \times 10^5$	$16^h40.316^m$	11.3	27.5	100 $_{-25}^{+10}$	90	75 $_{-10}^{+5}$	
			9.7	25.1				
			6.3	73				
1980S3	$1.51422 \times 10^5$	$16^h39.825^m$	3.3	57	90	40		
1980S26	$1.4170 \times 10^5$	$15^h05.08^m$	111		100			
1980S27	$1.394 \times 10^5$	$14^h42.72^m$	98	12	110			
1980S28	$1.373 \times 10^5$	$14^h25.77^m$	13.4	14	15	20	10 $^\dagger$	10 $^\dagger$

\*Resolution at which satellite size and albedo measurements have been made.  $^\dagger$ Axes B and C are not yet distinguishable for 1980S28.

about 210,000 to 300,000 km in radius. The E ring's visibility only in forward-scattered light supports observations of Terrile and Tokunaga (42) which indicate that it has a large component of small particles.

*Photometry of the rings.* Only a limited number of the Voyager ring observations have been photometrically calibrated, and thus only preliminary numbers for ring optical depth, particle albedo, and phase function can be presented at this time. Before discussing these results, we give a qualitative overview of the greatly varying appearance of the main rings with sun-ring-spacecraft geometry.

Before encounter, the lit face of the rings was observed at low phase angles ( $\sim 10^\circ$  to  $15^\circ$ ). The roughly equal brightness of the A and B rings and the low brightness of the rings relative to the planet are due to the low solar elevation angle ( $3.8^\circ$  at the time of encounter). After Voyager 1 passed through the ring plane to the unlit side, a quite different appearance of the rings was observed (Fig. 35). At this geometry the nearly totally opaque B ring and a variety of finer scale features appear relatively darker than the C ring and Cassini division. Regions of intermediate optical depth, such as the A ring, are intermediate in brightness. Truly vacant regions, such as the inner and outer gaps within the Cassini division and the Encke division, also appear dark due to the nearly total absence of scattering material.

During observations of the unlit face, viewing geometry allowed the rings to be seen against the bright limb of the planet, permitting determination of the optical depth of various regions (Fig. 32). After Voyager recrossed the ring plane and emerged to the lit face, the scattering geometry had changed and the rings were viewed at higher phase angles ( $130^\circ$  to  $160^\circ$ ). Regions characterized by strongly forward-scattering particles now appeared brighter than when viewed in backscatter before encounter (Fig. 36).

These variations of ring appearance with illumination and viewing geometry under the three general viewing conditions are summarized and illustrated in Fig. 37.

Images of the rings taken through various filters have been calibrated and reduced to  $I/F$  units (17), following the calibration procedure described by Soderblom *et al.* (64). Figure 38a illustrates radial photometric profiles from images taken through a green filter and an ultraviolet filter with a resolution of about 280 km/lp. The intensity scales are propor-

tional to  $I/F$ , but have been scaled so that the brightest parts of the B ring are at the same level for both filters. A marked difference in the two profiles is evident; the C ring and the material in the Cassini division are considerably brighter than the A and B rings in the ultraviolet than in the green filter image.

Figure 38b shows relative spectral reflectance at five spectral bandpasses (scaled to unity at green) for portions of the A, B, and C rings and the Cassini division. The A and B rings show essentially the same spectral properties, while the C ring and Cassini division show enhanced reflectance in the ultraviolet

and the violet. Also shown in Fig. 38b are ground-based data for the B ring (65). The agreement indicates that the camera characteristics have not changed dramatically since Jupiter encounter. Trial calculations indicate that the large difference in reflectance at shorter wavelengths for the C ring and Cassini division is not due to multiple scattering in regions of different optical depths. It is probably due to intrinsic differences in the optical properties of the ring particles, with the C ring and Cassini division particles having a more neutral (less red) color.

The azimuthal asymmetry of the A

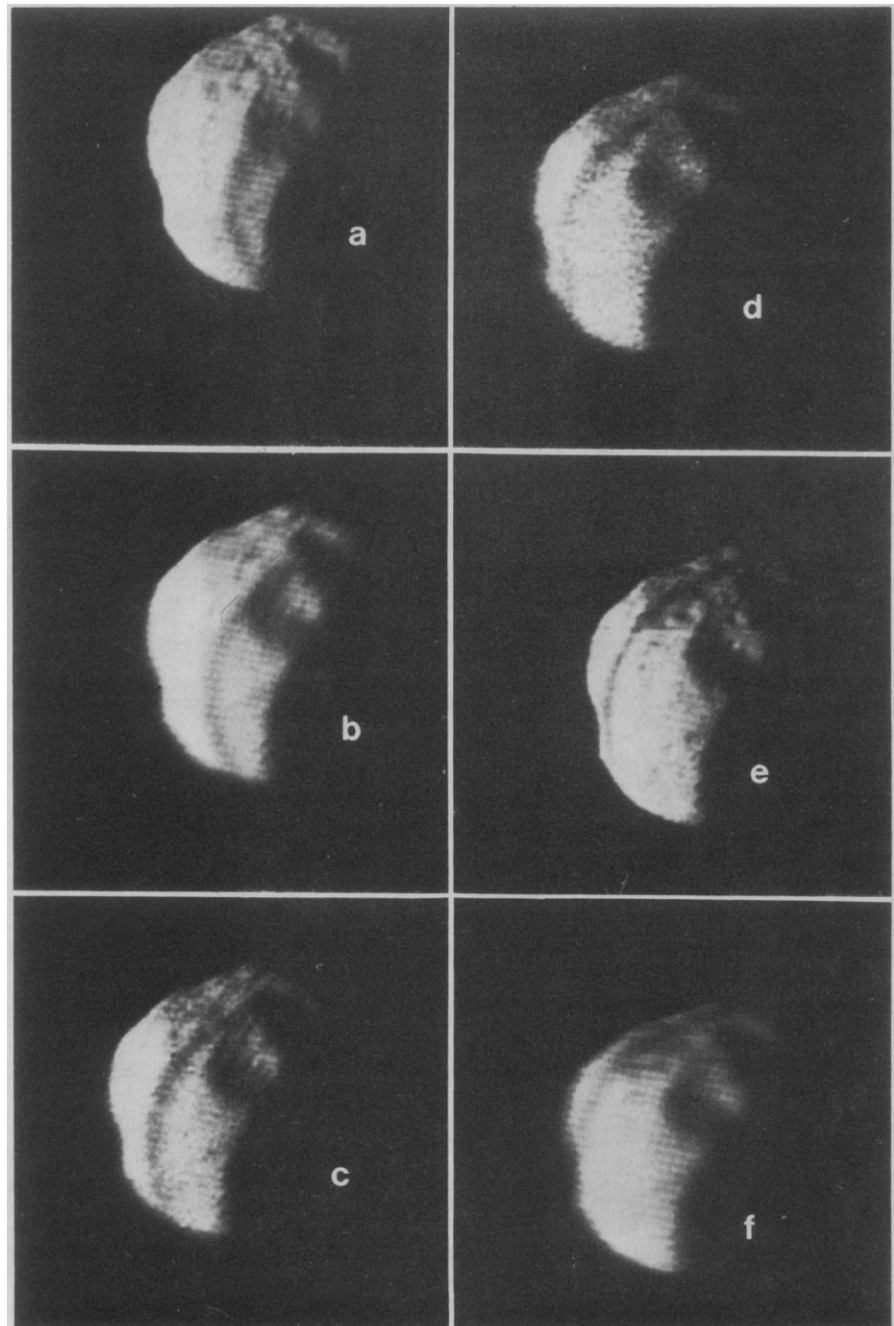


Fig. 29. Shadow of the F ring seen in transit across 1980S3. Images a to f were taken with various filters and exposure times and are separated in time by 3.2 minutes.

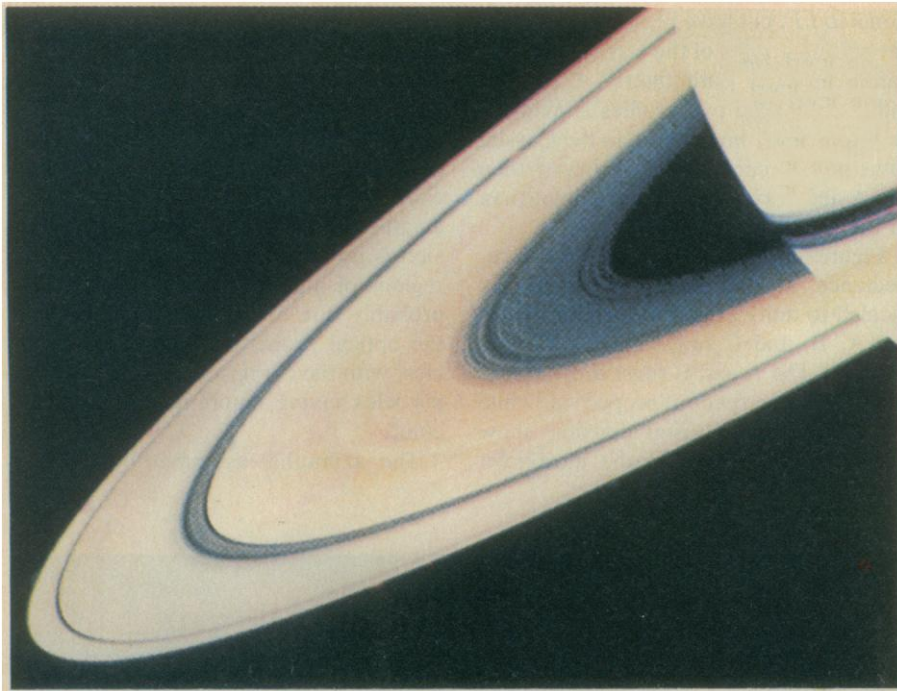


Fig. 30. False-color image of Saturn's rings. This image, recorded at a range of  $18 \times 10^6$  km, was constructed with ultraviolet, blue, and green filters used as blue, green, and red, respectively. A marked difference can be seen in the photometric properties of the C ring and Cassini division compared to the A and B rings. The colored "spokes" seen faintly in the B ring result from the lapse between camera shutterings of the images.

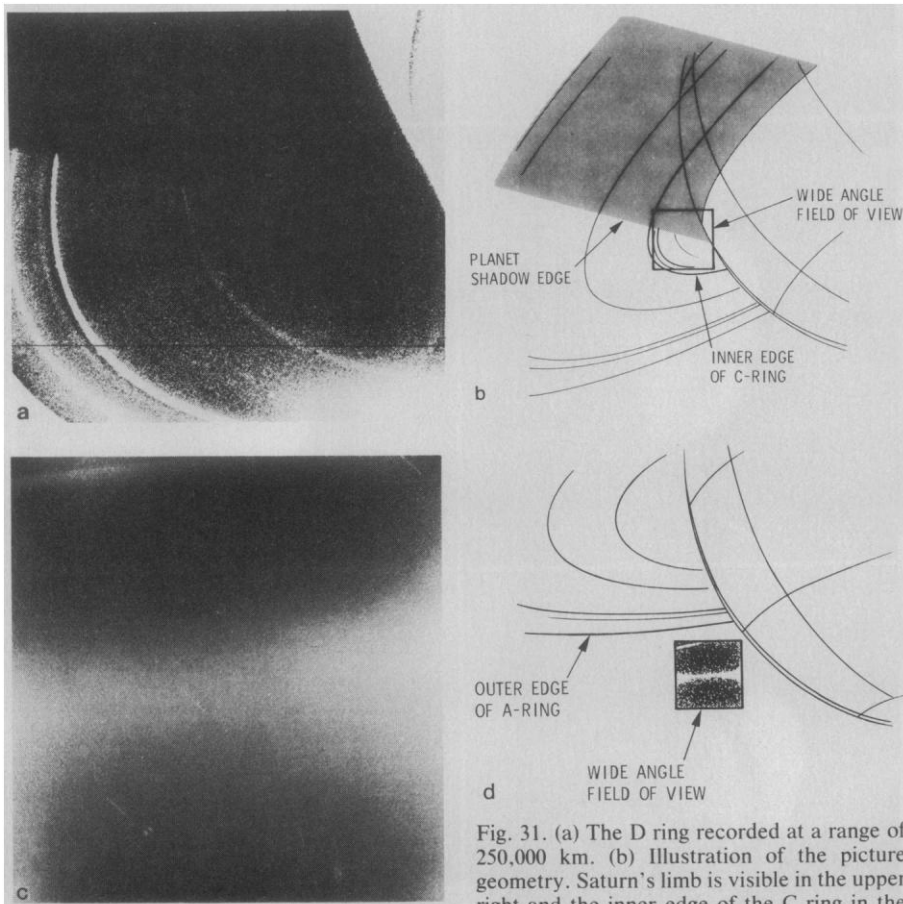


Fig. 31. (a) The D ring recorded at a range of 250,000 km. (b) Illustration of the picture geometry. Saturn's limb is visible in the upper right and the inner edge of the C ring in the lower left. Saturn's shadow cuts diagonally across the D ring. This faint ring is composed of several bands where ring particles are concentrated. The phase angle was  $157^\circ$ . (c) The G and E rings, with the image geometry shown in (d). The G ring appears as a faint and narrow feature about 168,000 km from Saturn's center. Image smear has broadened the ring's appearance. Also visible as a diffuse bright band is the E ring. This feature does not show sharp edges but appears to extend from about 210,000 to 300,000 km from Saturn. The phase angle was  $160^\circ$ .

ring observed from the ground (66) is also seen in Voyager 1 preencounter images of the ring system. Preliminary measurements on images taken 25 days before encounter at a resolution of 600 km/lp indicate that the modulation of ring brightness has approximately the same amplitude in all colors (blue, green, orange, and violet) and is comparable to the ground-based value, a peak-to-peak variation of  $\sim 15$  percent. The phase angle for the Voyager measurements was  $12^\circ$ , larger than is possible from Earth, with a viewing (ring-opening) angle of  $11^\circ$ . The phase of the variation with azimuth seen from the spacecraft exactly matches that seen from Earth. Minima in brightness occur in postconjunction quadrants at  $\sim 20^\circ$  from the ansae and maxima occur in preconjunction quadrants  $\sim 40^\circ$  from the ansae.

We made preliminary radiative transfer model calculations of the variation of ring brightness with viewing geometry and compared them with calibrated Voyager data. The radial regions used (Table 4) are not particularly heterogeneous and average values were used. Optical depths were obtained from calibrated data in Fig. 32 by differencing brightness across the limb of the planet (67).

The brightness of the limb was obtained from unobscured images at comparable latitudes and phase angles. No meaningful optical depth can be obtained for the B ring due to the dominance of light transmitted through a small fraction of narrow gaps, as inferred from Pioneer 11 photometry (67). However, its average optical depth is a more relevant quantity for diffuse brightness calculations and is sufficiently large ( $> 1$ ) to have a negligible effect on brightness calculations for the lit face.

It was realized before encounter (68) that the rings, especially the A and B rings, were more strongly backscattering than previously suspected. A phase function for Lambert spheres was assumed for initial computations, and a doubling code was used which treated the rings as having a bimodal distribution of optical depths, inferred from Pioneer 11 data (67). The small inhomogeneity thus introduced does not significantly affect the model brightness values shown. Typical results are shown in Fig. 39. The low phase angle data were used to obtain particle scattering albedos, which are given in Table 4, and refer to the clear filter of the wide-angle camera, with center wavelength  $\sim 5070 \text{ \AA}$ . The value given for the A and B rings is in excellent agreement with that obtained from ground-based observations and analyses (69). The particles in the C ring

and Cassini division are significantly darker than the A and B ring particles. The scattering phase function of the A and B ring particles is not satisfactorily matched by the Lambert sphere assumption. This may be seen by comparing the brightness of these regions observed at high phase angles (Fig. 37) with that observed at low phase angles. The high phase angle data fall at significantly lower albedo values, implying that the A and inner B ring particles are significantly more backscattering than Lambert spheres, a result consistent with the strong opposition brightening exhibited by many planetary bodies and particles with porous surfaces. The behavior of the outer B ring is not the same as that of the inner B ring; it is more forward-scattering than Lambert spheres. We have not yet attempted more detailed modeling of the particle phase functions. Interestingly enough, the C ring and Cassini division particles agree much better with the Lambert sphere assumption over the whole range of phase and viewing angles. Obviously, much refinement and expansion of these results must occur before detailed conclusions can be drawn about the nature of the particles in various regions.

*The C ring.* The structure of the C ring is regularly ordered and cannot be readily associated with gravitational resonances. Its inner edge, for instance, is not in correspondence with any predicted resonance location. A prominent gap several hundred kilometers wide at about 77,300 km does agree fairly well in location with an apsidal resonance with Titan (70, 71). Intermediate regions of the C ring show a low-contrast, undulating pattern. In the outer regions, an even more prominent gap  $\sim 270$  km wide is flanked in a regular and symmetrical manner by several relatively featureless bands that are more opaque than their surroundings and have sharp edges. This gap contains a narrow ringlet that is eccentric, as shown graphically in Fig. 33.

The outer gap is at a radius of about 87,100 km and the eccentric ringlet is 35 km wide and 100 km from the outer edge of the gap at its periapse. The ringlet is optically thick when viewed against Saturn's disk. At the apapse the ring is 90 km wide and 50 km from the outer edge of the gap. The ring has one periapse and one apapse, indicating that its eccentricity is not induced by resonance with an outer satellite. The line of apsides was not observed to move over a period of several days. This is consistent with a long precession period ( $\sim 24$  days) for the eccentric ring, probably due to the

quadrupole moment of Saturn. It seems likely that this ringlet must continually have its eccentricity forced by some mechanism, probably by a small satellite or satellites in its vicinity. Such forcing would seem to argue for an external resonance, but this feature is located near only a 2:1 resonance with the tiny

satellite 1980S28. This feature will be studied by Voyager 2.

In highest resolution (10 km/lp) images of the unlit face of the rings, the inner C ring exhibits many marginally resolved dark features, which are not as common in the outer C ring. The optical thickness of these features is not yet known. The

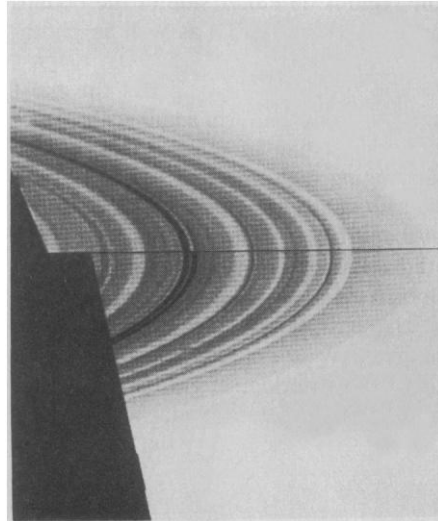


Fig. 32 (left). Wide-angle image showing the unilluminated side of Saturn's ring crossing in front of Saturn's bright limb. The C ring, B ring, Cassini division, and A ring are seen from bottom to top. Optically thick portions of the rings are viewed as dark regions crossing the limb. The left portion of the image is illuminated by light diffusely transmitted through optically thin but not empty regions

of the rings. Fig. 33 (right). High resolution (60 km/lp) composite view of the outer portion of the C ring. The horizontal line through the center marks the border between two photos; at the top is the trailing ansa of the rings and at the bottom the leading ansa. The dark gap in the center of both images shows a bright ringlet. This feature is eccentric and appears narrow in the lower image and slightly broader and displaced within the gap in the upper image.

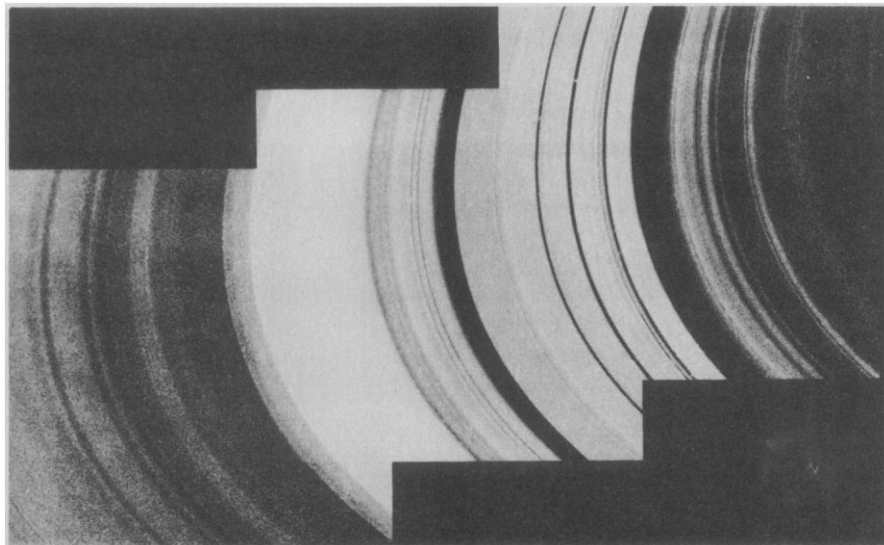


Fig. 34. This mosaic of the Cassini division seen in diffuse transmission was recorded as part of a larger ring scan with a resolution of about 10 km/lp. The Cassini division and the inner portion of the A ring appear bright because of their relatively lower optical depth than the A and B rings. Dark (and nearly empty) gaps are seen on either side of the Cassini division. A faint wavelike pattern can be seen on the brightest portion at the inner A ring.

C ring has also been observed at high phase angle ( $150^\circ$ ), and does not exhibit any significant brightening as would be expected from substantial quantities of small particles.

*The B ring.* The extremely sharp boundary between the B and C rings does not show any gap, nor does it correspond in location to any significant resonance. However, the properties of the regions on either side of the boundary differ structurally as well as photometrically.

In general, the B ring has the most extensive and uniform small-scale structure, consisting of many sequences of alternating high and low optical depth, with characteristic radial scales of several hundred to tens of kilometers. In transmission, narrow radial gaps of low optical depth are seen to be spaced irregularly, but with spacing comparable to their own widths of tens of kilometers. In forward scattering, bright bands several hundred kilometers wide are defined much more clearly than in backscatter

(Fig. 37). Locally regular structure is much more evident in forward scattering than in backscatter. In fact, these bands are so extensive and numerous as to cause the entire outer B ring on the average to brighten considerably in forward scattering. The inner B ring does not exhibit such forward-scattering behavior.

On a scale of  $10^3$  to  $10^4$  km, the B ring is divided into four radial zones of roughly equal width that differ qualitatively in photometric properties. The inner zone contains the most numerous and transparent gaps. Near the innermost edge the ring tends to be more opaque and to resemble the extremely opaque outer third quarter. These similar regions of low transparency have fewer narrow gaps. In general, the most opaque regions have the greatest brightening in forward-scattered light. They also exhibit the bulk of the "spoke" activity, discussed below in greater detail. Here we point out that the spoke features show the same increased brightness and defini-

tion as do the regions of the rings with which they are primarily associated, and are therefore characterized by a substantial number of small particles relative to surrounding areas.

*Cassini division.* The outer edge of the B ring is the inner edge of the Cassini division, and is quite opaque and abrupt to the limit of resolution. The boundary appears to correspond to the location of the 2:1 Mimas resonance, which is a resonance of major strength and has long been believed to be associated with the Cassini division. Figure 34 is a three-frame mosaic of the Cassini division, representing a small fraction of the Voyager 1 radial coverage of the entire ring system at  $\sim 10$  km/lp.

In general, these observations allow us to understand discrepancies in boundaries assigned to the Cassini division from ground-based, Pioneer 11, and preencounter Voyager 1 observations. A bright band  $\sim 1400$  km wide lies outward of the outermost prominent dark region, which is an essentially vacant gap  $\sim 170$  km wide. This bright region, when viewed from above, is comparable in brightness to the A ring and appears to blend with it. When seen from the unlit face, however, it appears comparable to the C ring in opacity ( $\sim 0.1$ ). Therefore, if matter density is the basic criterion for distinguishing regions, it should be regarded as part of the Cassini division, which was essentially the conclusion reached by the Pioneer 11 photopolarimeter team (4). However, the lit-face brightness argues for particle properties similar to those of the A ring, so that if local particle properties are considered the basic criterion, the region should be regarded as part of the A ring.

A very regular sequence of alternating bright and dark features extends practically throughout this interesting (bright band) region, with interval decreasing outward, typically hundreds to tens of kilometers. This pattern may be evidence for density waves within the ring material, with dark areas of concentration and bright areas of rarefaction. Between the two prominent gaps lie four or five bands of similar appearance, each with fine structure at the limit of our resolution. This set of bands was used to produce the photometric results for the Cassini division discussed earlier. Within the inner of the two gaps is a narrow ringlet similar in width, opacity, and eccentricity to the ringlet in the outer gap of the C ring described earlier. We expect that resonant forcing maintains the eccentricity of this ringlet. Its proximity to the Mimas 2:1 resonance makes it of special interest for observations by Voy-

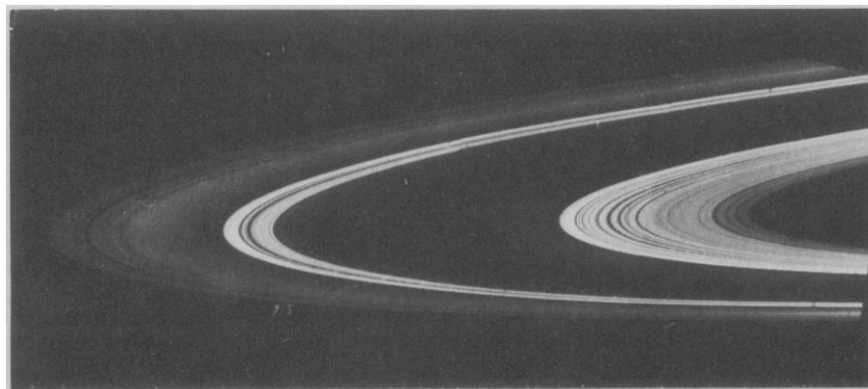


Fig. 35. Mosaic showing the dark side of the rings. Optically thin regions like the C ring and Cassini division appear brighter than the more optically thick regions of the A and B rings due to diffuse scattering of transmitted light. Dark ring features are either areas of high optical depth or nearly empty gaps.

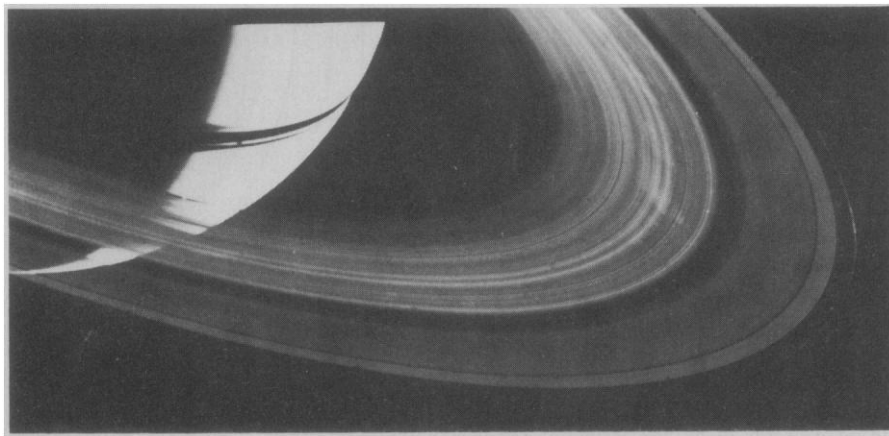


Fig. 36. Outbound mosaic of the illuminated side of the rings recorded at a phase angle of  $132^\circ$ . Regions of the rings that appear bright in forward-scattered light are thought to have a significant component of small (micrometer-sized) particles. These regions include the F ring, portions of the A and B rings, and, in particular, the spokelike features in the B ring.

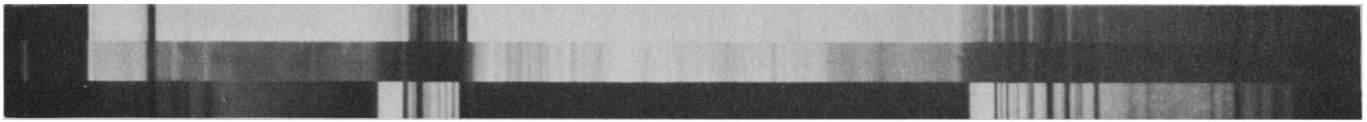


Fig. 37. Composite showing three radial slices through the rings at three different viewing geometries. (Top) Illuminated side in backscattered light; (middle) same side in forward-scattered light; (bottom) unilluminated side in backscattered light. Due to foreshortening, the horizontal scale includes nonlinearities, causing some mismatch of features in three perspectives. Radial distance from Saturn increases to the left.

ager 2. Finally, images obtained at large phase angles show that the Cassini division in general does not have a substantial component of small, forward-scattering particles. In this respect as well, it is similar to the C ring.

*The A ring.* The inner edge of the A ring is as abrupt as the B/C boundary and as opaque as any region of the B ring. Most of the A ring, however, is of lower optical depth and varies smoothly in brightness. The Encke division, at a radial distance of 133,200 km, is vacant except for two very narrow, faint ringlets that are irregularly clumped. These ringlets are brighter in forward scattering and probably contain a significant fraction of small particles.

Although the Mimas 5:3 resonance is nearby, it corresponds better with one of five other features of great interest in the outer A ring. These features are generally dark in backscatter (Fig. 40), bright in forward scatter (Fig. 36), and optically thick relative to surrounding areas. At high resolution (Fig. 41) they exhibit

alternating bright and dark patterns with a spacing of tens of kilometers. It should be noted that there are far more theoretical resonances with the external satellites than there are ring features in this region. Perhaps the superposition of two or more resonances is required for their formation. Four of these features are close to four positions where calculated resonances nearly coincide. The remaining feature shows an unusual and intriguing effect in forward scattering; whereas the other features are bright compared to their surroundings, this feature reverses contrast at the ansa. This suggests vertical relief at this radius, which tentatively corresponds to the 5:3 resonance with Mimas' orbital inclination involving the orbital inclination of the ring particles.

Outward of the Encke division, there is a pattern of unresolved A ring features that are dark in backscatter, bright in forward scatter, and decrease in interval with increasing radius. These features may represent a sequence of classical resonances converging on one of the

close-in satellites. The entire region outside the Encke division is ~ 25 percent brighter than the region inside; this is echoed by a region at the outer edge of the A ring, several hundred kilometers wide, that is set off from the A ring by an apparently vacant gap tens of kilometers wide and is ~ 50 percent brighter in forward scatter than the region immediately inside the gap (see Fig. 37). The outer edge of the A ring is sharp at the limit of our resolution.

*The F ring.* Pioneer 11 discovered the narrow F ring about 3600 km outside the edge of the A ring (4). As Voyager 1 approached Saturn two satellites were discovered in close association with the F ring (Fig. 42). Outside the ring, 1980S26 moves in an eccentric orbit that takes it between 2000 and 500 km from the ring. Just 500 km inside the ring is 1980S27, which is comparable in size to 1980S26 (about 200 km in diameter). The F ring was also found to be eccentric, with at least a 400-km variation in its 140,000-km radius. It is not known

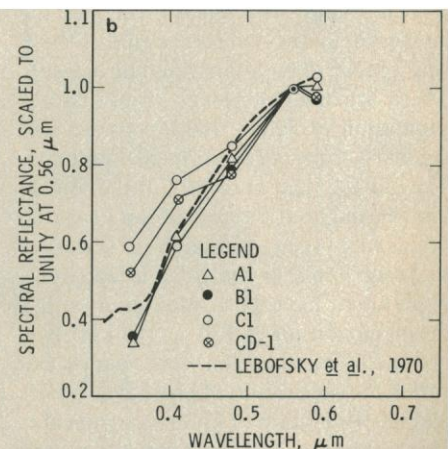
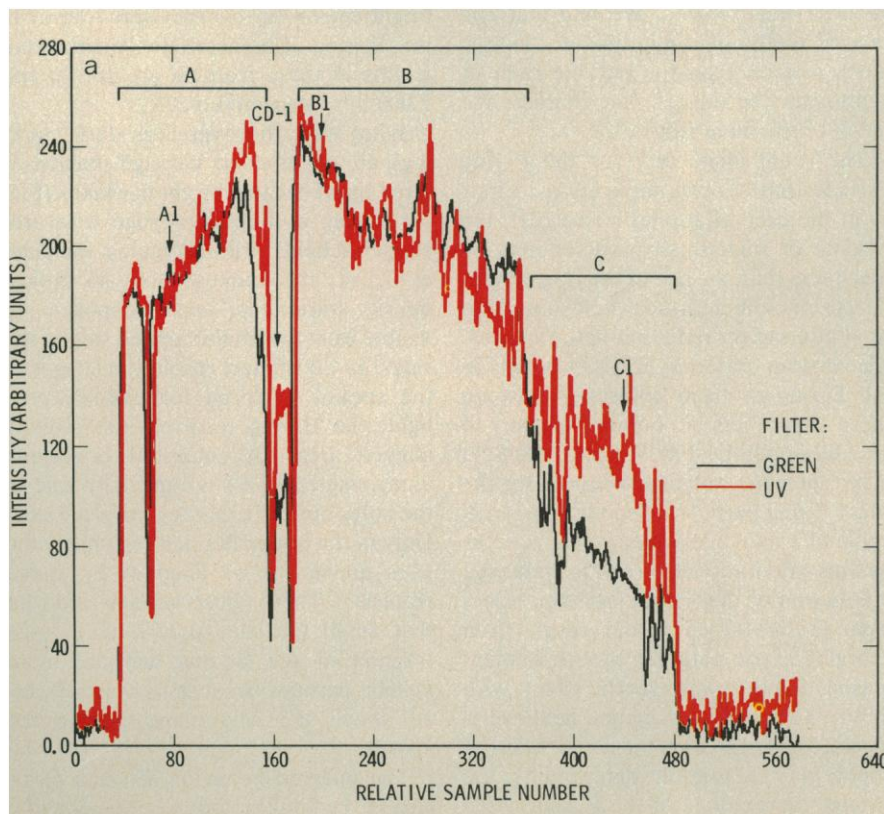


Fig. 38. (a) Two photometric radial profiles of one ring ansa. The dark line is from an image taken through a green filter (effective wavelength,  $0.56 \mu\text{m}$ ) and the red line from an ultraviolet ( $0.35 \mu\text{m}$ ) image. Intensity is in arbitrary units proportional to  $I/F$  but scaled for comparison between the two wavelengths. Relative sample number gives distance in internal frame units, which are geometrically calibrated and linear. Arrows mark locations from which relative spectral reflectances are given in (b). (b) Relative spectral reflectance (scaled to unity at  $0.56 \mu\text{m}$ ) for the portions of the ring marked in (a). Also shown are ground-based data for the B ring (65).

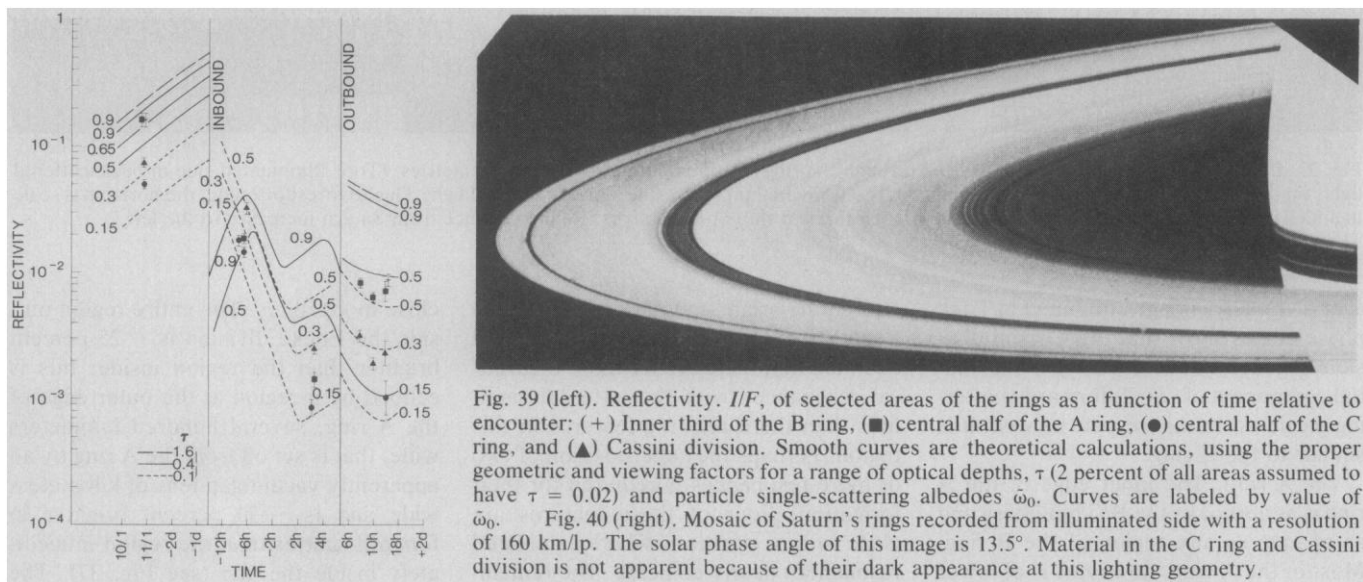


Fig. 39 (left). Reflectivity,  $I/F$ , of selected areas of the rings as a function of time relative to encounter: (+) Inner third of the B ring, (■) central half of the A ring, (●) central half of the C ring, and (▲) Cassini division. Smooth curves are theoretical calculations, using the proper geometric and viewing factors for a range of optical depths,  $\tau$  (2 percent of all areas assumed to have  $\tau = 0.02$ ) and particle single-scattering albedoes  $\bar{\omega}_0$ . Curves are labeled by value of  $\bar{\omega}_0$ . Fig. 40 (right). Mosaic of Saturn's rings recorded from illuminated side with a resolution of 160 km/lp. The solar phase angle of this image is  $13.5^\circ$ . Material in the C ring and Cassini division is not apparent because of their dark appearance at this lighting geometry.

whether the precession of satellite orbits and F ring eccentricities will change the close-approach distances of the F ring and 1980S26 and 1980S27.

In high-resolution images, bright clumps are seen in the F ring. Their orbital motion, determined by tracking from frame to frame, coincides with the F ring's Keplerian period of about 15 hours. Still higher resolution [Fig. 43 (left)] shows that the F ring has three components, each about 20 km wide. The inner component is the faintest; it is smooth and does not appear to interact with the other two. Perhaps the most startling view acquired by Voyager 1 is shown in Fig. 43 (right). Over half the image, the outer two components of the F ring appear to be intertwined or braided. There are five crossover points with a separation of  $700 \pm 100$  km (mean and standard error of four measurements). The radial extent of the braids is about 30 km. Throughout the rest of the image no braids are seen, although a series of kinks or knots in the rings is apparent. Nine knots have been measured with a mean separation of  $630 \pm 150$  km. It is not clear whether the coincidence between the separation of crossover points and the separation of knots is significant. If it is, then  $\sim 700$  km seems to be the characteristic scale length for warps in the F rings. The complex nature of the F ring braids and clumps is most likely connected with the gravitational actions of the "shepherding" satellites, 1980S26 and 1980S27. The limited viewing geometries and times did not permit three-dimensional characterization of the features or their time evolution. These parameters, to be measured by Voyager 2, and details of the satellites and ring eccentricities are needed to describe F ring

gravitational dynamics. Why the third (faintest) component appears smooth and without knots or kinks still remains to be explained.

At high phase angles, the F ring and particularly the ring clumps become brighter, indicating a significant component of small particles. We estimated the (cross section-weighted) average radius  $\bar{r}$  of the particles by comparing the brightness at phase angles of  $140^\circ$  and  $155^\circ$ . Assuming that the F ring is optically thin, it suffices to consider only single scattering. Also, Mie theory may be used, since the single-scattering phase function is insensitive to particle shape at these small angles. We find that  $\bar{r}$  is several tenths of a micrometer. This is much smaller than the particle radii of centimeters to meters that characterize much of the main rings (72).

The small value of  $\bar{r}$  for the F ring particles has several implications. First, as in the case of Jupiter's ring (73), the lifetime of such small particles may be much less than the age of the ring system due to micrometeoroidal collisions and/or sputtering by radiation belt particles. Ejecta from cratering of larger bodies in the F ring or from collisions between these hypothetical bodies (perturbed gravitationally by 1980S26 and 1980S27) may represent a plausible source for the small F ring particles. Second, the small value of  $\bar{r}$  may allow electromagnetic as well as gravitational forces to influence the motion of the F ring particles. Electromagnetic forces would result from charging of the particles by the ambient plasma and the photoelectric effect, with Saturn's corotating magnetic field exerting a Lorentz force on them. Such forces could play a role in determining the strange morphology of the F ring.

*Spokes.* Among the most interesting variable ring features are the narrow radial markings or spokes in the B ring. These features were first observed as dark wedge-shaped projections rotating in the outer half of the ring, predominantly on the morning ansa (the part of the ring just emerged from Saturn's shadow). At high resolution, spokes were easily observed on both ansae and across most of the B ring. Spokes have not been seen to cross the Cassini division and seldom extend farther in than about 105,000 km from the center of Saturn. This point appears to be a sharp cutoff for most of the spokes and is a bright region (in backscattered light) in the B ring. Characteristic lengths and widths of these features are 10,000 and 2,000 km, respectively.

What were discovered as dark markings during inbound passage (backscattered light) became bright markings (Fig. 44) during outbound passage (forward-scattered light). Viewed against the planet's disk, the spokes show no optical density variations, and no spokes are visible from the unilluminated side of the rings. In the highest resolution images of the spokes taken in forward-scattered light, the B ring resolves into radially aligned areas of enhanced brightness along ringlets. This is especially true in the outer optically thin region of the ring. Only in the optically thick regions do the gaps appear to be filled in by spoke material. These observations indicate that small particles constitute a large fraction of the B ring and are more visible, perhaps because they are elevated above the ring plane, within the spokes.

The inferred behavior of small particles in the spokes and the presence of a

rotating magnetic field in the ring environment suggest a possible connection between electromagnetic forces and the dynamics of spoke rotation. Spoke motion was measured by comparing images of the rings taken over 30-minute intervals. Figure 45 shows data from two sets of images, one inbound and one outbound, on which spokes are seen on the morning ansa. Rotation rate is plotted against radial distance from Saturn's center and curves representing pure Keplerian motion and the rotation of Saturn's magnetic field are shown for comparison.

These data seem to lie along the Keplerian line, most convincingly at radial distances greater than  $\sim 10.7 \times 10^4$  km. Although large morphological changes in the spokes are not apparent over an interval of 30 minutes, the diffuseness of these features makes exact determination of their location difficult, particularly at smaller radii, where they are more diffuse. Still, it appears that along most of the length of a spoke, motion is independent of the magnetic field.

The difference between Keplerian and magnetic orbital motion grows as one moves away from a radius of  $112.5 \times 10^3$  km (Fig. 45). Hence it is interesting to note that the spokes commonly appear wedge shaped, wider toward Saturn, and that the location at which they become the narrowest coincides with the point where Keplerian orbital motion and magnetic angular ve-

locity are identical. Also, examination of many images indicates that the vast majority of spokes are near-radial or tilting away from radial in such a way that Keplerian motion will continue to tilt them further. These observations suggest that the magnetic field is responsible for creation of the spokes and that Keplerian motion is responsible for their particle dynamics. The characteristic wedge shape may reflect the difference between Keplerian and magnetic orbital motion over the time it takes one spoke feature to be created.

The modulating influence of Saturn's magnetic field could also account for the random occurrence of spokes on the rings. The Voyager 1 radio astronomy experiment (9) detected electrostatic discharge signatures that are believed to originate in the rings and have a modulation period similar to the magnetic field rotation rate. Spokes may be the visible manifestation of these phenomena. Correlation of radial alignment of the spokes with a particular magnetic longitude has not yet been investigated.

Finally, the spokes do not seem to have any common orbital longitude of origin in the ring system. Spoke alignment with the radial direction does not seem to be correlated with any particular orbital location. When pure Keplerian motion was assumed and spoke features were "mapped" backward in time to check for alignment with the morning or evening edge of Saturn's shadow on the

ring plane, the features were found not to be parallel to the shadow.

*Discussion.* Out of the great complexity of Saturn's rings, we can only begin to draw general conclusions. Qualitative differences exist between the classical main ring elements. The C ring and Cassini division are similar in color and albedo and unlike the A and B rings in these properties. Although there are possible mechanisms for varying the surface properties of ring particles as a function of optical thickness (thickness variations could result in shading variations), there does not seem to be an unambiguous pattern in the data. The rings also differ in abundance of small, forward-scattering particles, with the outer B ring, the F ring, the outermost A ring, and the discrete features surrounding the Encke division having the highest relative abundance. The Cassini division and the C ring show the least evidence of such small particles, and they show less backscatter relative to Lambert spheres than do the A and B ring particles. The low abundance of small particles in the C ring and Cassini regions implies that the bluer color of these regions is an intrinsic compositional effect and not due to small-particle Rayleigh scattering behavior. The A and C rings lack the disordered structure evident in the many narrow transparent zones in the B ring; they exhibit a relatively smooth background punctuated by discrete features, sometimes located at classical resonances (A

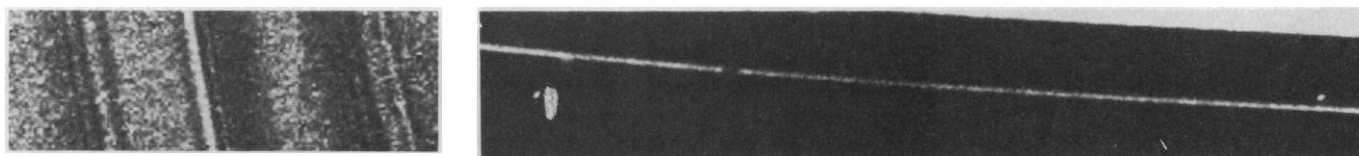


Fig. 41 (left). Detail of part of the A ring seen in diffusely transmitted light with a resolution of about 10 km/lp. The outer part of the rings is to the left. Visible are some of the wavelike patterns seen near strong ring features. These patterns may be evidence for density waves produced in the rings near strong satellite resonances. Fig. 42 (right). Segment of the F ring, showing the positions of the neighboring satellites 1980S26 (left) and 1980S27 (right). The outer edge of the A ring is visible in the upper right. It has been suggested (72) that the gravitational effects of the inner and outer satellites can confine the ring particles into a narrow structure. The eccentric motion of these satellites may also be responsible for the complicated structure in the F ring. The bright area on the edge of the A ring and the two diffuse areas in the F ring are artifacts.

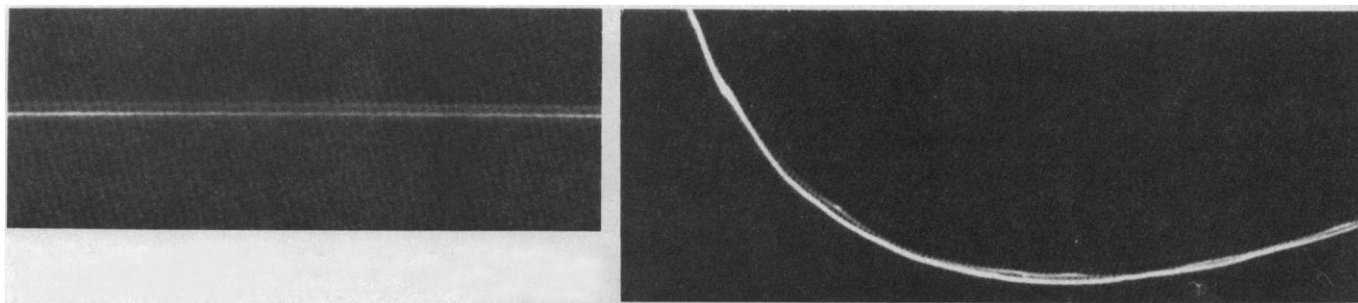


Fig. 43. Two sections of the F ring. On the left, the ring appears as three parallel components with a slight longitudinal variation in brightness. The image on the right shows a different area with a very complex structure. The two outer components appear to cross several times, giving the ring a braided appearance. Several brighter clumps or knots in the ring are also visible.

ring) and sometimes not (A and C rings).

The boundaries between the rings seem to represent real differences in particle properties. The greater abundance of small particles in certain regions implies local differences in rates of production, as small particles are short-lived. The F ring and outer A ring are likely to be locations of relatively more intense collisions due to the perturbing activity of 1980S26, 1980S27, and 1980S28. Thus it is not surprising to find many small particles there. The B ring exhibits both a preponderance of small particles and a preponderance of narrow gaps. Both phenomena are consistent with a relatively large number of large (~ 1 km) moonlets in the B ring. Such moonlets will clear gaps ~ 10 km wide around themselves by superposition of torques (71) in a time approximately equal to the diffusion collapse time of such gaps. The gravitationally deposited energy produced by such large particles will then produce large random-collision velocities (74) and consequently greater production rates of small particles. The spoke patterns, representing increased visibility of small particles, are restricted to regions that are already rich in small particles. In the A ring, the fact that many small particles are seen in association with the regularly spaced features

near the Encke division is consistent with the idea that the features are density waves, forced by gravitational resonances with 1980S26 and 1980S27 or some other objects, that become nonlinear as they propagate from their source, producing vigorous collisions and numerous small particles. The many unresolved features outside the Encke division may be of similar origin.

Several significant questions remain. If the presence of small, forward-scattering particles is indicative of vigorous local dynamics, why are such particles absent from the Cassini division, the location of some of the strongest predicted dynamical activity? If the simultaneous presence of many narrow gaps and many small particles, widely dispersed, is indicative of the presence of many embedded and invisible kilometer-size moonlets, how does one understand the presence and predominance of such objects in the B ring? How are the distinct and abrupt boundaries between the main rings themselves, and the significant qualitative differences in particle properties between the classical regions, maintained? At present, these boundaries are not satisfactorily correlated with any possible classical gravitational resonances, except for the boundary between the outer B ring and the inner

Cassini division. While the sharp outer edge of the A ring is understood, the sharp inner edge of the C ring is not.

BRADFORD A. SMITH

*Department of Planetary Sciences,  
University of Arizona, Tucson 85721*

LAURENCE SODERBLOM

*U.S. Geological Survey,  
Flagstaff, Arizona 86001*

RETA BEEBE

*Department of Astronomy,  
New Mexico State University,  
Las Cruces 88003*

JOSEPH BOYCE

GEOFFERY BRIGGS

*NASA Headquarters,  
Washington, D.C. 20546*

ANNE BUNKER

STEWART A. COLLINS

CANDICE J. HANSEN

TORRENCE V. JOHNSON

JIM L. MITCHELL

RICHARD J. TERRILE

*Jet Propulsion Laboratory,  
Pasadena, California 91109*

MICHAEL CARR

*U.S. Geological Survey,  
Menlo Park, California 94025*

ALLEN F. COOK II

*Center for Astrophysics,  
Cambridge, Massachusetts 02138*

JEFFREY CUZZI

JAMES B. POLLACK

*NASA/Ames Research Center,  
Moffett Field, California 94035*

G. EDWARD DANIELSON

ANDREW INGERSOLL

*Division of Geological and Planetary  
Sciences, California Institute of  
Technology, Pasadena 91125*

MERTON E. DAVIES

*Rand Corporation,  
Santa Monica, California 90406*

GARRY E. HUNT

*University College London,  
London WC 1E 6BT, England*

HAROLD MASURSKY

EUGENE SHOEMAKER

*U.S. Geological Survey, Flagstaff*

DAVID MORRISON

*Institute for Astronomy,  
University of Hawaii, Honolulu 96822*

TOBIAS OWEN

*Department of Earth and Space  
Sciences, State University of  
New York, Stony Brook 11790*

CARL SAGAN

JOSEPH VEVERKA

*Cornell University,  
Ithaca, New York 14853*

ROBERT STROM

*Lunar and Planetary Laboratory,  
University of Arizona*

VERNER E. SUOMI

*University of Wisconsin,  
Madison 53706*

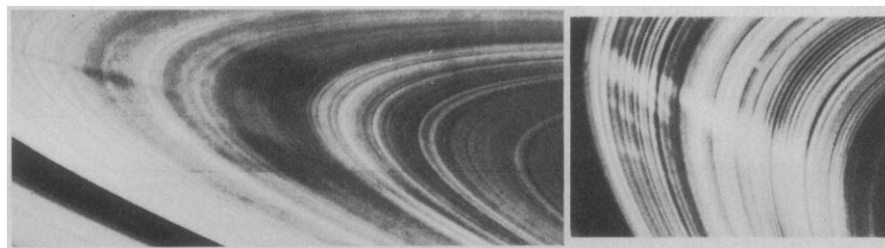


Fig. 44. Views of the B ring in (left) backscattered and (right) forward-scattered light. The backscatter image shows several spoke features as dark regions. They are broadest and most prominent near the center of the ring. In forward scattering, the contrast is reversed and the spokes appear as bright features. In this geometry the concentric structure in the B ring is seen with increased contrast, accentuating hundreds of light and dark ringlets.

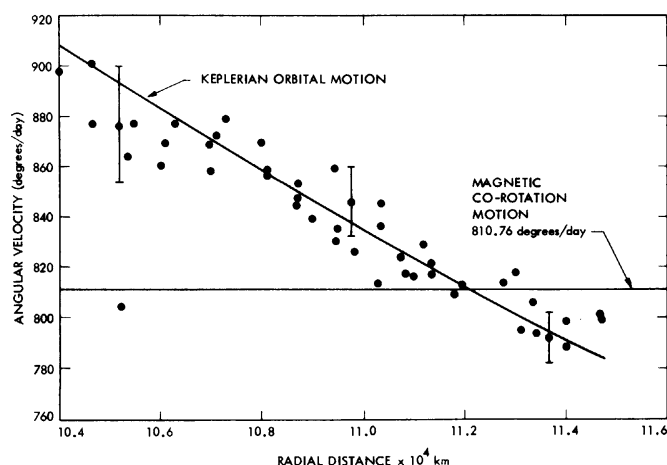


Fig. 45. Measurements of the angular velocity of spoke features in the B ring plotted against radial distance. Three images, recorded 30 minutes apart, were used for the measurements. The points fall on a line coinciding with the predicted angular motion for particles in Keplerian orbits. Also shown is the angular velocity of the corotating magnetic field of Saturn. Typical measurement error bars are shown at various radii.

## References and Notes

1. C. Huygens, *Systema Saturnium* (Adrian Vlacq, The Hague, 1659).
2. A. F. O'D. Alexander, *The Planet Saturn: A History of Observation, Theory and Discovery* (Dover, New York, 1962).
3. B. Smith *et al.*, *Space Sci. Rev.* **21**, 103 (1977).
4. T. Gehrels *et al.*, *Science* **207**, 434 (1980).
5. G. M. Yagi, J. J. Lorre, P. L. Jepsen, in *Proceedings of a Conference on the Atmospheric Environment of Aerospace Systems and Applied Meteorology* (American Meteorological Society, Boston, 1978), pp. 110-117.
6. Man-Computer Interactive Data Acquisition System (MCIDAS), an interactive image processing system used for measurement of tie point or cloud pattern correlation-derived wind speeds.
7. R. F. Beebe, A. P. Ingersoll, G. E. Hunt, J. L. Mitchell, J.-P. Muller, *Geophys. Res. Lett.* **7**, 1 (1980); A. P. Ingersoll, R. F. Beebe, J. L. Mitchell, G. W. Garneau, G. M. Yagi, J.-P. Muller, *J. Geophys. Res.*, in press.
8. E. J. Reese, *Icarus* **15**, 466 (1971); D. Wenkert, J. A. Howell, A. P. Ingersoll, in preparation; Reese cites only confirmed observations of spots in Saturn's atmosphere; Wenkert *et al.* make use of a larger data set consisting of both confirmed and unconfirmed observations.
9. J. Warwick *et al.*, *Science*, **212**, 239 (1981).
10. R. Hanel *et al.*, *ibid.*, p. 193.
11. G. S. Orton and A. P. Ingersoll, *J. Geophys. Res.* **85**, 5871 (1980).
12. D. J. Stevenson and E. E. Salpeter, *Astrophys. J. Suppl. Ser.* **35**, 239 (1977).
13. S. L. Hess and H. A. Panofsky, in *Compendium of Meteorology*, T. F. Malone, Ed. (American Meteorological Society, Boston, 1951), p. 391.
14. G. P. Williams, *J. Atmos. Sci.* **36**, 932 (1979).
15. V. P. Starr, *Physics of Negative Viscosity Phenomena* (McGraw-Hill, New York, 1968), p. 69.
16. L. S. Slobokin, I. F. Buyakov, R. D. Cess, J. Caldwell, *J. Quant. Spectrosc. Radiat. Transfer* **20**, 481 (1978).
17. *IF* is the brightness relative to that of a 100 percent diffuse Lambert reflector, illuminated and viewed normally.
18. J. T. Bergstralh, G. S. Orton, D. J. Diner, K. H. Baines, J. S. Neff, M. A. Allen, *Icarus*, in press.
19. G. Tyler *et al.*; *Science* **212**, 201 (1981).
20. G. P. Kuiper, *Astrophys. J.* **100**, 378 (1944).
21. J. Comas Sola, *J. Br. Astron. Assoc.* **19**, 151 (1908).
22. J. Veverka, *Icarus* **18**, 657 (1973); B. Zellner, *ibid.*, p. 661.
23. J. Caldwell, T. Owen, A. Rivolo, V. Moore, G. E. Hunt, P. S. Butterworth, *Astron. J.*, in press.
24. C. Sagan, *Space Sci. Rev.* **11**, 73 (1971); *Icarus* **18**, 649 (1973); B. N. Khare and C. Sagan, *ibid.* **20**, 311 (1973); D. M. Hunten, Ed., *NASA Spec. Publ. SP-340* (1973); T. Owen, *Origins Life* **5**, 41 (1974); T. Scattergood and T. Owen, *Icarus* **30**, 780 (1977).
25. K. Rages and J. B. Pollack, *Icarus* **41**, 119 (1980).
26. J. B. Pollack and J. N. Cuzzi, *J. Atmos. Sci.* **37**, 868 (1980).
27. M. Tomasko, *J. Geophys. Res.* **85**, 5937 (1980).
28. P. Smith, *ibid.*, p. 5943.
29. L. Broadfoot *et al.*, *Science* **212**, 206 (1981).
30. A. B. Lutz, T. Owen, R. D. Cess, *Astrophys. J.* **203**, 541 (1976).
31. L. M. Traflet, *ibid.* **175**, 295 (1972).
32. D. M. Hunten, *NASA Conf. Publ. 2068* (1978), p. 127.
33. See, for example, C. Sagan, *Icarus* **10**, 290 (1969).
34. G. W. Lockwood, *ibid.* **32**, 413 (1977).
35. ———, personal communication.
36. C. Leovy and J. B. Pollack, *Icarus* **19**, 195 (1973); G. S. Golitsyn, *ibid.* **24**, 70 (1975).
37. D. P. Cruikshank, *Rev. Geophys. Space Phys.* **17**, 165 (1979); *NASA Conf. Publ. 2068* (1978), p. 217; D. Morrison, *Bull. Am. Astron. Soc.* **12**, 727 (Abstr.) (1980).
38. T. V. Johnson, G. J. Veeder, D. Matson, *Icarus* **24**, 428 (1975); D. Morrison *et al.*, *Astrophys. J. Lett.* **207**, 213 (1976); U. Fink *et al.*, *ibid.*, p. 63; R. N. Clark and P. D. Owensby, in preparation.
39. G. W. Null, E. L. Lau, E. D. Biller, J. D. Anderson, *Astron. J.*, in press.
40. C. F. Yoder, *Nature (London)* **279**, 767 (1979).
41. A. F. Cook and R. Terrile, in preparation.
42. R. Terrile and A. Tokunaga, *Bull. Am. Astron. Soc.* **12**, 701 (1980).
43. T. Owen, in preparation.
44. L. E. Andersson, thesis, Indiana University (1974).
45. S. J. Peale, in *Planetary Satellites*, J. Burns, Ed. (Univ. of Arizona Press, Tucson, 1977).
46. P. Bodenheimer, A. S. Grossman, W. DeCamplii, G. Marcy, J. B. Pollack, *Icarus* **41**, 293 (1980); A. S. Grossman, J. B. Pollack, R. T. Reynold, A. L. Summers, H. C. Graboske, Jr., *ibid.* **42**, 358 (1980).
47. J. Veverka, J. Burt, J. L. Elliot, J. Goguen, *ibid.* **33**, 301 (1978).
48. G. J. Veeder and D. L. Matson, *Astron. J.* **85**, 969 (1980).
49. A. F. Cook and F. A. Franklin, *Icarus* **13**, 282 (1970).
50. C. Peterson, *ibid.* **24**, 499 (1975).
51. E. M. Shoemaker and R. F. Wolfe, in *The Satellites of Jupiter*, D. Morrison, Ed. (Univ. of Arizona Press, Tucson, in press).
52. A. J. R. Prentice, *Phys. Lett. A* **80**, 205 (1980).
53. M. J. Lupo and J. S. Lewis, *Icarus* **40**, 157 (1979).
54. J. B. Pollack and P. T. Reynolds, *ibid.* **21**, 248 (1974).
55. J. B. Pollack, A. S. Grossman, R. Moore, H. C. Graboske, Jr., *ibid.* **29**, 35 (1976).
56. R. Moore, private communication.
57. A. Dollfus, *Astronomie* **6**, 253 (1968).
58. J. W. Fountain and S. M. Larson, *Icarus* **36**, 92 (1978).
59. Several new satellites of Saturn were suggested by dips in the charged-particle fluxes observed by Pioneer. It is possible that 1980S26 was detected by Pioneer in 1979; until the Pioneer trajectory data are reexamined, small discrepancies in the orbital radii cannot be resolved (60).
60. J. A. Van Allen, M. F. Thomsen, B. A. Randall, R. L. Rairden, C. L. Grosskreutz, *Science* **207**, 415 (1980); J. A. Simpson *et al.*, *J. Geophys. Res.* **85**, 5731 (1980).
61. The designations given here are temporary; 1980S1 refers to the first observation of an unknown satellite of Saturn in 1980. Because the coorbital satellites exchange orbits, it is not yet known which of the two observed in 1980 corresponds to the first (S10) and which to the second (S11) satellite recorded in the 1966 discovery images.
62. S. P. Synott, C. F. Peters, B. A. Smith, L. A. Morabito, *Science* **212**, 191 (1981).
63. P. Guerin, *C. R. Acad. Sci. Ser. B* **270**, 125 (1970); S. M. Larson, *Icarus* **37**, 399 (1979).
64. L. Soderblom *et al.*, *Geophys. Res. Lett.* **7**, 963 (1980).
65. L. A. Lebofsky, T. V. Johnson, T. B. McCord, *Icarus* **13**, 226 (1970).
66. K. Lumme and W. Irvine, *Astrophys. J.* **204**, LSS (1976); H. J. Reitsema, R. F. Beebe, B. A. Smith, *Astron. J.* **81**, 209 (1976).
67. L. W. Esposito, J. P. Dilley, J. W. Fountain, *J. Geophys. Res.* **85**, 5948 (1980).
68. S. A. Collins *et al.*, *Nature (London)* **288**, 439 (1980).
69. Y. Kawata and W. Irvine, in *Exploration of the Planetary System*, A. Wozcysk and C. Iwaniszewska, Eds. (Reidel, Dordrecht, Netherlands, 1974), p. 441.
70. D. Brouwer and G. L. Clemence, *Methods of Celestial Mechanics* (Academic Press, New York, 1981); E. W. Brown and C. A. Shook, *Planetary Theory* (Cambridge Univ. Press, Cambridge, England, 1933).
71. P. Goldreich and S. Tremaine, *Icarus* **34**, 240 (1978).
72. J. N. Cuzzi and J. L. Pollack, *ibid.* **33**, 233 (1978).
73. T. Owen, G. E. Danielson, A. F. Cook, C. Hansen, V. L. Hall, T. C. Duxbury, *Nature (London)* **281**, 442 (1979).
74. J. N. Cuzzi, J. A. Burns, R. H. Durisen, P. M. Hamill, *ibid.*, p. 202.
75. Exploration of the Saturn system has been possible only because of the unselfish aid of many of our colleagues over the past decade. With regard to our atmospheric dynamics investigation, we thank R. Krauss at the University of Wisconsin and J. P. Müller, V. Moore, and R. F. T. Barney at University College London for making independent measurements of zonal winds on Saturn. We thank D. Wenkert, K. Rages, and W. Drew for their comments and help in our studies of the atmospheres of Saturn and Titan. Our investigations into Saturn's rings have been aided by J. Burns, K. Bilski, L. Esposito, F. Franklin, P. Goldreich, R. Greenberg, C. Porco, J. Lissauer, D. Jewitt, F. H. Shu, and G. Yagi. We thank D. Pieri, J. Plescia, and S. Squyres for their help with the section on satellite geology. We greatly appreciate the dedication and invaluable aid of the Image Processing Laboratory (IPL), the Mission Test Imaging System (MTIS), the Voyager science integration team, sequence team, and spacecraft team, as well as the Photography Laboratory and Graphics Department, all at Jet Propulsion Laboratory. We especially thank J. Anderson, M. Brownell, L. Cullen, G. Dimit, E. Korsmo, P. Kupferman, and F. Meng for help in sequence planning, exposure calculations, and image processing. The preparation of this manuscript benefited significantly from the assistance of L. Garcia, V. Nelson, G. Paterson, L. Pieri, O. Raper, and D. B. Weir. Finally, we thank our reviewers, including D. M. Hunten and M. J. S. Belton, for their helpful comments. G.E.H. is supported by the Science Research Council, Great Britain. This report presents the result of one phase of research carried out at Jet Propulsion Laboratory under NASA contract NAS 7-100.

11 February 1981; revised 24 February 1981

## Orbits of the Small Satellites of Saturn

**Abstract.** *Orbital parameter values and associated uncertainties determined from Voyager 1 imaging data for the satellites 1980S1, 1980S3, 1980S6, 1980S26, 1980S27, and 1980S28 are presented.*

Six small satellites were observed during the approach of Voyager 1 to Saturn; three were known from ground-based observations (1-4) and three were discovered in the Voyager images (5). The "co-orbital" satellites 1980S1 and 1980S3 (6) were observed first approximately 75 days before encounter on the basis of predictions by B. A. Smith, H. J. Reitsema, and J. Fountain (7). The intervals for the remaining four are considerably shorter, ranging from about 20 days for 1980S6 and 1980S27 to approximately 8 days for 1980S28.

In order to refer their positions to the center of Saturn, 1980S1, 1980S3, and 1980S6 were recorded over the entire observing interval in frames in which at least one pointing reference, either a star or one or more of the satellites Mimas,

Enceladus, Tethys, Dione, and Rhea, also appeared. The orbital parameter values of these large satellites were also improved during approach by using hundreds of satellite-star frames taken primarily for spacecraft navigational purposes. Observations of 1980S26, 1980S27, and 1980S28 were then referred to the center of Saturn by using stars and/or the orbits of the large satellites as well as 1980S1 and 1980S3.

Since orbits were nearly singular, some of the parameters actually estimated were combinations of the usual classic set. In particular, the parameters  $h$ ,  $k$ ,  $p$ , and  $q$  (8) were estimated:

$$\begin{aligned} h &= e \sin \omega \\ k &= e \cos \omega \\ p &= \tan i/2 \sin \Omega \\ q &= \tan i/2 \cos \Omega \end{aligned}$$